



Efficient Low-Reynolds-Number Airfoils

Lance W. Traub* and Cory Coffman†

Embry Riddle Aeronautical University, Prescott, Arizona 86301

DOI: 10.2514/1.C035515

A low speed wind tunnel investigation is presented characterizing the effect of leading and trailing edge flaps on thin flat plate airfoils at low Reynolds numbers. Flap size and setting angle were varied. Tests were conducted at Reynolds numbers of 40,000, 60,000, and 80,000, consistent with the operational regime of micro aerial vehicles. Performance was contrasted against a circular arc profile and three conventional airfoils. Testing encompassed force balance and surface pressure measurement. The numeric data were complemented by on and off surface flow visualization as well as the development of an analytic prediction model. The results indicate that the deployment of leading and trailing edge flaps can significantly improve the airfoil's efficiency—not just compared with a flat plate but also a 5% camber circular arc profile. For the tested geometries, a leading and trailing edge flap angle of 15 deg was optimal. Conventional airfoil performance degraded significantly at low Reynolds numbers, yielding efficiencies far below any of the flat plate airfoils for $Re = 40,000$ and $60,000$. Increasing the Reynolds number to 80,000 showed a dramatic improvement in the performance of the conventional airfoils.

Nomenclature

a, b, c	=	coefficients, Eq. (3)
C_d	=	sectional drag coefficient
C_l	=	sectional lift coefficient
$C_{l\max}$	=	maximum lift coefficient
C_{la}	=	lift curve slope
C_m	=	pitching moment coefficient
C_p	=	pressure coefficient
c	=	chord
k	=	drag due to lift constant
x	=	chordwise coordinate
α	=	angle of attack
γ, β	=	corrections, Eq. (10)
δ	=	flap angle
θ	=	transformation variable
η	=	attainable leading edge thrust

Subscripts

LE	=	leading edge
max	=	maximum
md	=	minimum drag
min	=	minimum
TE	=	trailing edge
ZL	=	zero lift
0	=	zero angle of attack

I. Introduction

ENABLING technology to support the development of unmanned aerial vehicles has promoted a sustained research effort to characterize and understand low-Reynolds-number flows. The term “low Reynolds number” is somewhat nebulous, but in the present context pertains to incompressible flows that have marked viscous dependence. The Re realm of micro aerial vehicles (MAVs) and small birds is typically between 10^4 and 10^5 , whereas $Re < 10^4$ is typically the domain of insects [1,2]. Large birds, moderate-size unmanned aerial vehicles, and hobbyist radio-controlled aircraft often operate at $10^5 < Re < 10^6$.

Low-Reynolds-number flows are often defined by the state of the boundary layer and the behavior of boundary-layer separation. For $Re < 5 \times 10^4$ (note that this value is highly dependent on operational conditions, including free stream turbulence, airfoil surface condition, etc.), the boundary layer is laminar and resistant to disturbances that may promote transition [3]. As a result, adverse pressure gradients that are encountered by the laminar boundary layer readily cause laminar separation without subsequent transition; thus shear layer re-attachment is not realized. Consequently, this flow regime is defined by large-scale open separation, low lift coefficients, and high drag coefficients; airfoil efficiency is inherently low.

An increase in Reynolds number facilitates transition of the separated shear layer. Tollmein–Schlichting waves/disturbances originating from the attached upstream boundary layer and consequently embedded within the separated shear layer may grow exponentially yielding transition [4], promoted by the adverse pressure gradient increasing the shear layer receptivity to a wide range of disturbance frequencies. Transition may also be facilitated by an inflectional instability in the shear layer. The separated layer is also sensitive to the Kelvin–Helmholtz instability, causing the layer to roll up into discrete vortices [5,6]. The breakdown of these vortices then promotes turbulence [5]. Subsequent entrainment/mixing of the higher-momentum free-stream into the shear layer thickens the layer and re-energizes it such that momentum is transported toward the surface. Ensuing flow re-attachment yields a flow structure that is referred to as a laminar separation bubble (LSB), as first noted by Jones [7]. The shear layer re-attachment location is generally not steady but tends to oscillate, caused by the shedding of vortical structures from the bubble [8]. Bubbles profoundly affect airfoil aerodynamics; they may create nonlinearities in the lift curve [9,10] associated with their movement, and they increase sectional pressure drag by increasing the momentum thickness of the re-attached boundary layer (the re-attached boundary layer is thicker than what would result in an attached flow transition process). The bubble generally forms toward the aft extent of the airfoil at low angles of attack and then moves forward and contracts with increasing angle of attack [9]—a behavior driven by the increasing adversity of the pressure gradient and its concomitant effect on the location of separation and initiation/promotion of transition.

As demonstrated by biological evolution, the Avian airfoil solution within the Reynolds number domain of MAVs is that of a thin highly cambered airfoil [11,12]. As presented by Withers [11] and Oehme and Kitzler [12] birds ranging in size from a swift to a hawk have thickness-to-chord ratios of 3.5 to 6.8% and peak cambers ranging from 3.9 to 11.2% of the chord. Wind tunnel tests have shown that simple flat plates readily outperform conventional airfoil sections for $Re < 80,000$ [13]. The flow field associated with a thin flat plate is different from that of a conventional airfoil. The boundary layer that arrives at the leading edge (LE) of the plate from the lower stagnation

Received 8 March 2019; revision received 8 May 2019; accepted for publication 14 May 2019; published online Open Access 11 July 2019. Copyright © 2019 by Lance W. Traub. Published by the American Institute of Aeronautics and Astronautics, Inc., with permission. All requests for copying and permission to reprint should be submitted to CCC at www.copyright.com; employ the eISSN 1533-3868 to initiate your request. See also AIAA Rights and Permissions www.aiaa.org/randp.

*Professor, Aerospace Engineering Department. Senior Member AIAA.

†Undergraduate Research Student, Aerospace Engineering Department.

point is laminar. Aerodynamically, the thin sharp LE would theoretically impose an infinite adverse pressure gradient on the boundary layer trying to negotiate it. Thus, the sharp LE causes an extremely high adverse pressure gradient that not only enforces separation but rapidly promotes shear layer transition [14]. Through mixing and entrainment of the freestream, the shear layer is energized and grows, facilitating upper surface turbulent re-attachment in the form of a long bubble originating from the LE. An increase in angle of attack causes an increase in the length of the bubble [14,15]. Coincidence of the bubble re-attachment point with the trailing edge (TE) often coincides with the maximum lift coefficient [14]. Cambering the flat plate (circular arc profile) yields further aerodynamic improvement and a profile that is more akin to that of a bird wing. A study by Okamoto et al. [16] suggested that a circular arc profile of approximately 5–6% camber may be optimal in terms of achieving a high lift-to-drag ratio, a similar result to that in Ref. [13].

Flapped flat plates have been examined prior [17–19], with application to airfoils for efficient supersonic performance (as wave drag is lessened by reducing thickness). A study by Cahill et al. [17] varied the setting angle of both LE and TE flaps on symmetric circular arc sharp-edged plates (the upper and lower profile of the airfoils were circular arcs) for Re ranging from 3 to 9 million. Their data showed that deflection of a TE flap could reduce drag due to lift. Deflection of a LE flap further compounded the drag reduction. In all instances, flap deflection increased the $C_{d\min}$. TE flaps have also been shown to reduce the drag due to lift on both slender and nonslender delta wings [20,21]. The drag reduction mechanism is a reduced angle of attack to achieve a given lift coefficient; consequently the aft component of the normal force coefficient is reduced.

There appears to be little study of the effect of leading and trailing flaps on a flat plate at low Reynolds numbers ($< 10^5$). This geometry may prove equivalent or superior to a circular arc airfoil, is simpler to manufacture, and could also be variable (i.e., flap angles could be altered). Consequently, this paper provides a comprehensive experimental database characterizing the effect of LE and TE flaps on a thin flat plate at $Re = 40,000$, 60,000, and 80,000. The majority of the testing was conducted at $Re = 60,000$ using the LE and TE flaps in various setting angle combinations. The most efficient of these geometries was then tested at $Re = 40,000$ and 80,000. Three conventional airfoils as well as a 5% circular arc airfoil were also evaluated at these three Reynolds numbers and compared with the flapped plates. A semi-empirical analytic prediction method, based on thin airfoil theory, is also developed to estimate the lift-dependent drag of the flapped airfoil geometries. Force balance, surface flow visualization, surface pressure measurement, and off surface streamlines are used as diagnostics tools.

Table 1 Nominal and measured trailing edge flap setting angles ($\delta_{LE} = 0$ deg)

δ_{TE} (nominal), deg ($x_{TE}/c = 0.8$)	δ_{TE} (measured), deg ($x_{TE}/c = 0.8$)
5	4.7
10	9.9
15	15.2
20	20.3

Table 2 Nominal and measured leading edge flap setting angles ($\delta_{TE} = 15$ deg)

δ_{LE} (nominal), deg	δ_{LE} (measured), deg ($x_{LE}/c = 0.1$)	δ_{LE} (measured), deg ($x_{LE}/c = 0.15$)	δ_{LE} (measured), deg ($x_{LE}/c = 0.2$)
10	10.1	10.2	10.1
15	15.0	14.9	15.1
20	19.4	20.1	20.3
25	24.7	25.1	24.7

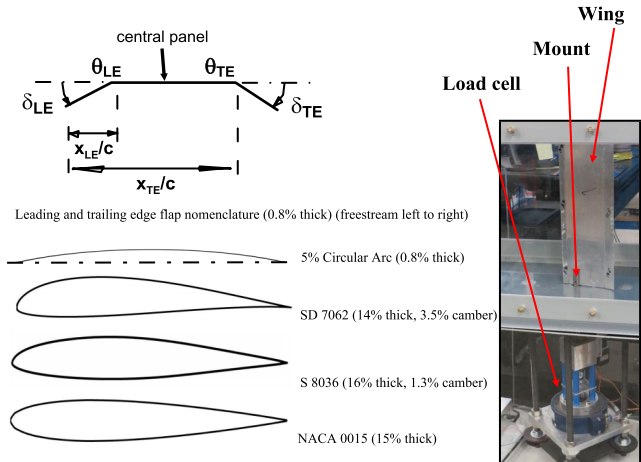


Fig. 1 Airfoil profiles, geometry definitions, and model installation.

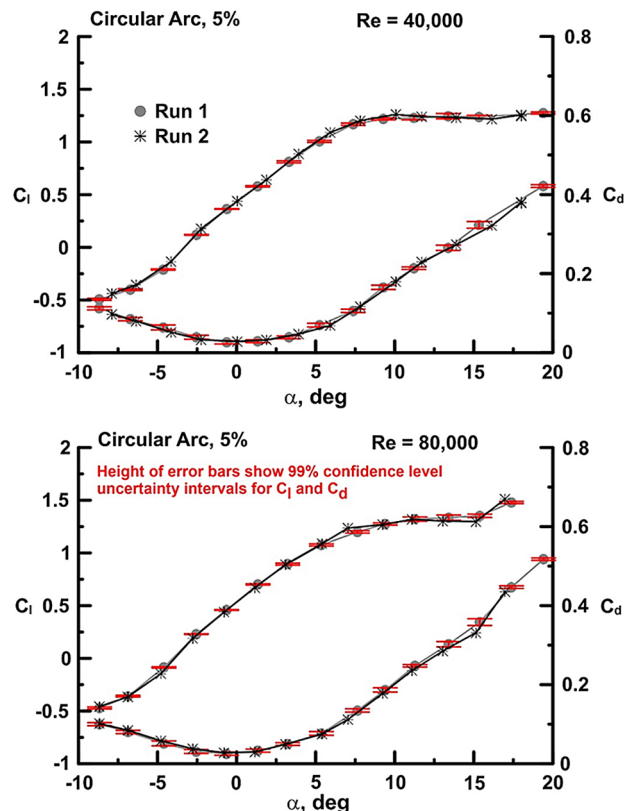


Fig. 2 Wind tunnel data repeatability, 5% camber circular arc profile.

II. Equipment and Procedure

The wind-tunnel models were manufactured from a thin (0.8 mm) aluminum plate. They were cut to size and then bent to the required angle. The models had a chord of 100 mm and a span of 304 mm; consequently the thickness-to-chord ratio was 0.8%. The models were mounted such that they spanned the wind tunnel with a 0.4 mm

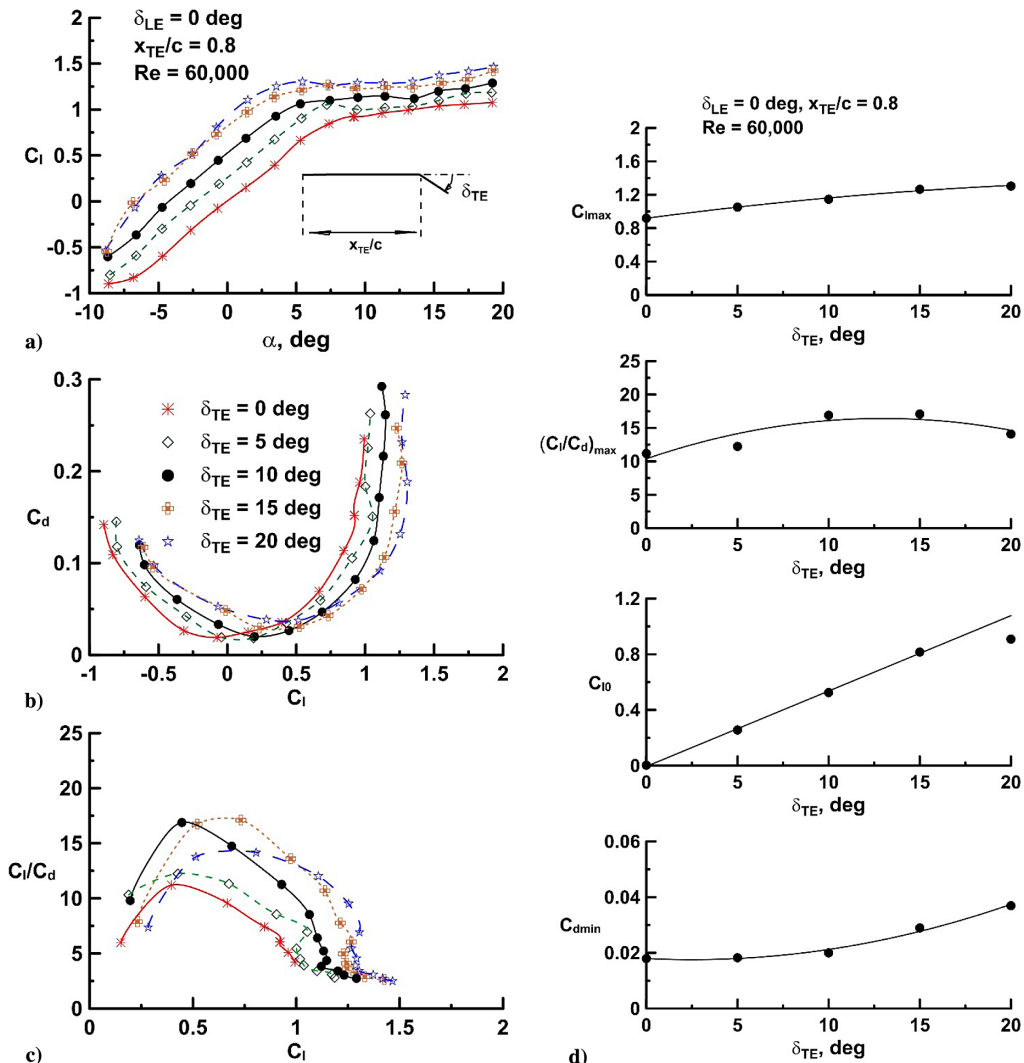


Fig. 3 Effect of trailing edge flap angle on measured a) lift, b) drag, c) lift-to-drag ratio, and d) data summary.

gap between the tip and the wind tunnel wall. For all tests where employed, the length of the TE flap was 20 mm, or 20% of the chord. LE flap extents of 10, 15, and 20% of the chord were evaluated. Tables 1 and 2 summarize the geometric setting angles of the LE and TE flaps, while Fig. 1 clarifies the nomenclature. For all LE flap settings, the TE flap was set to 15 deg. Shown is the nominal and measured flap angles, caused by difficulty in bending the plates to the exact required angle (Tables 1 and 2). For all data presentation, the nominal angle is used for simplicity.

The flat plate and the optimal airfoil ($x_{LE}/c = 0.15$, $\delta_{LE} = 15$ deg, $x_{TE}/c = 0.8$, $\delta_{TE} = 15$ deg) were also pressure tapped using 27–30 taps (depending on the airfoil) for each surface. The taps were 0.25 mm in diameter and were located along a diagonal arranged at 40 deg to the chord line. Pressures were measured using an in-house 60-port electronic pressure scanner. Data were acquired at a rate of 250 kHz with each presented point representing the average of 1000 samples. Calibration of this instrument against a primary standard (Amatek PKII deadweight tester) showed accuracy within 1 Pa for each port.

A 5% camber circular arc airfoil was also fabricated from the 0.8 mm aluminum plate. Conventional airfoils with NACA 0015, S8036, and SD 7062 profiles were also manufactured (rapid prototyped in acrylonitrile butadiene styrene) for comparison testing. These airfoils had the same planform dimensions as the aluminum plate airfoils and were finished by sanding with 1000- and 1200-grit sand paper. See Fig. 1 for the airfoil profiles. All pitching moments

were recorded around the airfoil's quarter chord. Wall corrections were not applied to the data due to the comparative nature of the study.

Tests were conducted at Reynolds numbers of 40,000, 60,000, and 80,000 (freestream velocities of 7.2, 10.8, and 14.4 m/s, respectively) as these values span the typical operational envelope for a MAV. Wind tunnel trials were conducted in Embry Riddle Aeronautical University's 304.8 mm by 304.8 mm open-circuit low-speed wind tunnel. This facility has a measured turbulence intensity of 0.24% in the velocity range spanning the wind tunnel tests. Variation of velocity within the flow is less than 1% of the average freestream. Flow angularity across the freestream is within 0.1 deg. A six-component JR3 load cell was used to measure the loads. A comparison of measured loads with those applied in calibration has shown accuracy within 0.015 N (corresponding to $\Delta C_l = 0.02$ for the worst-case scenario, $Re = 40,000$). Repeated data measurements indicated an average uncertainty interval (for a 99% confidence level) of 0.002 and 0.0032 for C_l at low and high angles of attack, respectively; values were similar for C_d . The angle-of-attack setting accuracy is within ± 0.05 deg. The wind tunnel models were attached to the load cell using a small mount that affixed with screws (see Fig. 1). Interference between the mount and the wings was negligible.

Surface flow visualization was undertaken using a mixture of kerosene, oil, and ultraviolet dye marker. The oil mixture was brushed onto the airfoil and the wind tunnel was rapidly brought up to velocity. Both still and video images were recorded for later analysis.

Streamlines were visualized using a thin high-resistance wire suspended ahead of the airfoil. The wire was coated with glycerin and then heated, causing streamline rendering through glycerin vapor.

III. Results and Discussion

A. Repeatability

Accuracy and repeatability of low-Reynolds-number tests is always a concern, caused by the very small magnitude of the imposed loads. Consequently, Fig. 2 shows a typical repeated data run (shown for the 5% circular arc profile) for $Re = 40,000$ and $80,000$. Repeatability for both C_l and C_d is excellent for both test cases. Error bars (for run 1) calculated for each presented data point and representing a 99% confidence level are also shown. Note that the width of the error bars is for clarity of presentation and is not indicative of the uncertainty of angle of attack.

B. Trailing Edge Flaps

The effect of TE flaps on the measured C_l and C_d is shown in Fig. 3. Tests were undertaken at $Re = 60,000$ using a 20% chord flap length. Deflecting a TE flap is seen to cause a systematic and proportional negative shift of α_{ZL} ; that is, α_{ZL} is proportional to δ_{TE} as is well-documented for TE flaps [22,23] (although this is not seen for $\delta_{TE} = 20$ deg, probably due to excessive separation off the flap

reducing effectiveness; Fig. 3a). The maximum lift coefficient is also observed to increase with flap angle. As is documented for thin plates [14], stall of the long bubble type is very docile with an unpronounced $C_{l\max}$. Increasing δ_{TE} affects the drag coefficient in two ways: increasing the drag polars' minimum C_d and shifting $C_{d\min}$ to higher lift coefficients (see Fig. 3b). The net effect is a significant increase in airfoil efficiency (caused by the shift of C_{lmd}), represented by the lift-to-drag ratio (Fig. 3c). Deflecting the TE flap to 15 deg yields an increase in peak C_l/C_d of 52.7% compared with the flat plate airfoil. The peak efficiency occurs at a higher lift coefficient as δ_{TE} increases; caused by the increase of $C_{d\min}$ and C_{lmd} [24]. The drag decrease produced by TE flap deflection is caused by a reduction in the required angle of attack of the airfoil to produce a given C_l [20,21]. As a result, the aft component of the normal force is reduced and outweighs the drag increment caused by the flap itself.

A summary of aerodynamic parameters identifiable in Figs. 3a–3c is shown in Fig. 3d. The maximum lift coefficient shows a monotonic increase with δ_{TE} within the range examined; $\delta_{TE} = 20$ deg achieves a 42% increase in $C_{l\max}$ compared with the flat plate. The maximum lift-to-drag ratio has a parabolic dependency on δ_{TE} , with a peak centered around $10 \leq \delta_{TE} \leq 15$ deg. Nonlinearity in the lift curve, which is common at low Re , complicates the identification of the zero lift angle of attack. An analogous defining camber-based parameter is C_{l0} , the zero-angle-of-attack lift coefficient (noting that $C_{l0} = -C_{la}\alpha_{ZL}$). It follows from thin airfoil theory [25] that C_{l0}

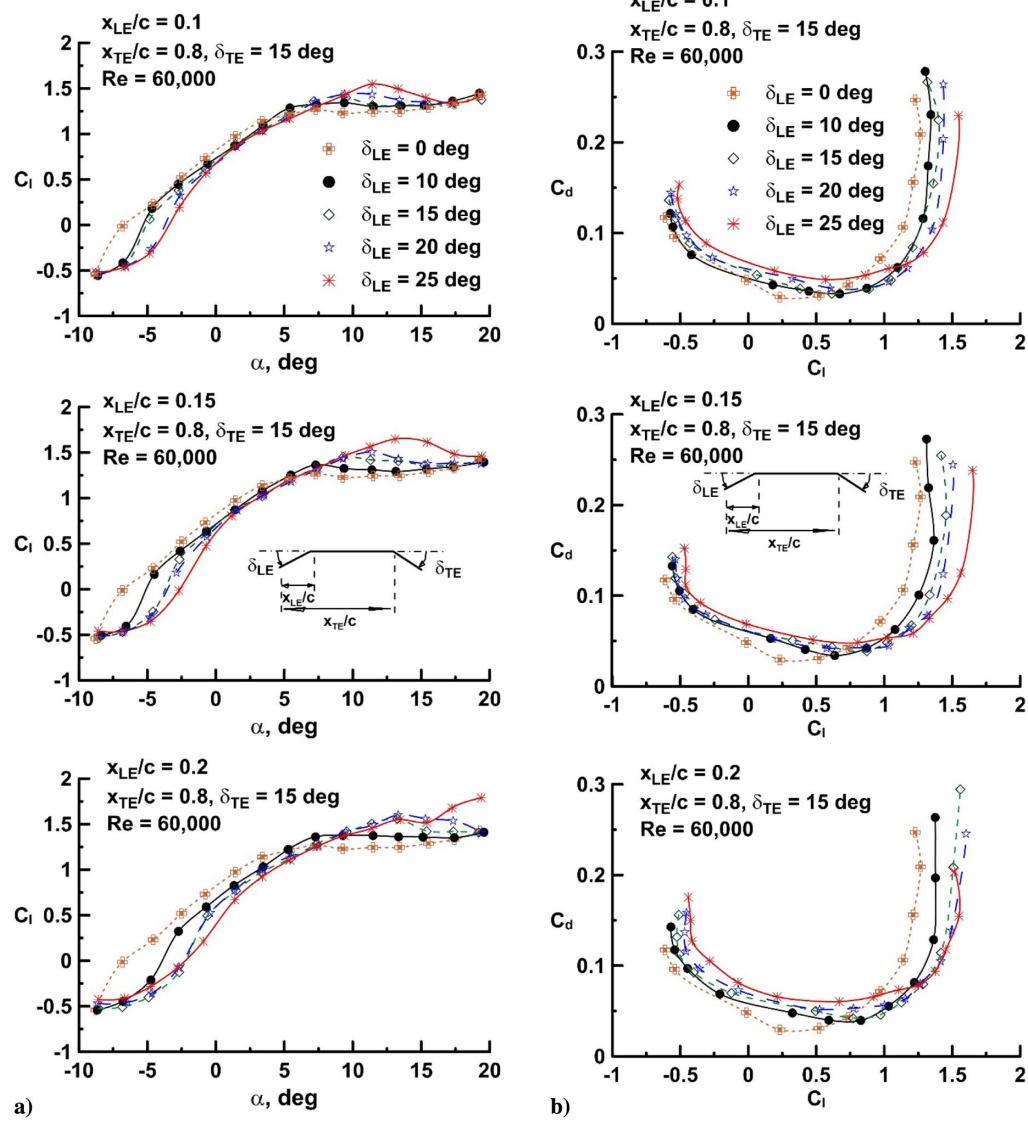


Fig. 4 Effect of δ_{LE} and flap length on the measured a) lift, b) drag, c) lift-to-drag ratio, and d) pitching moment coefficient.

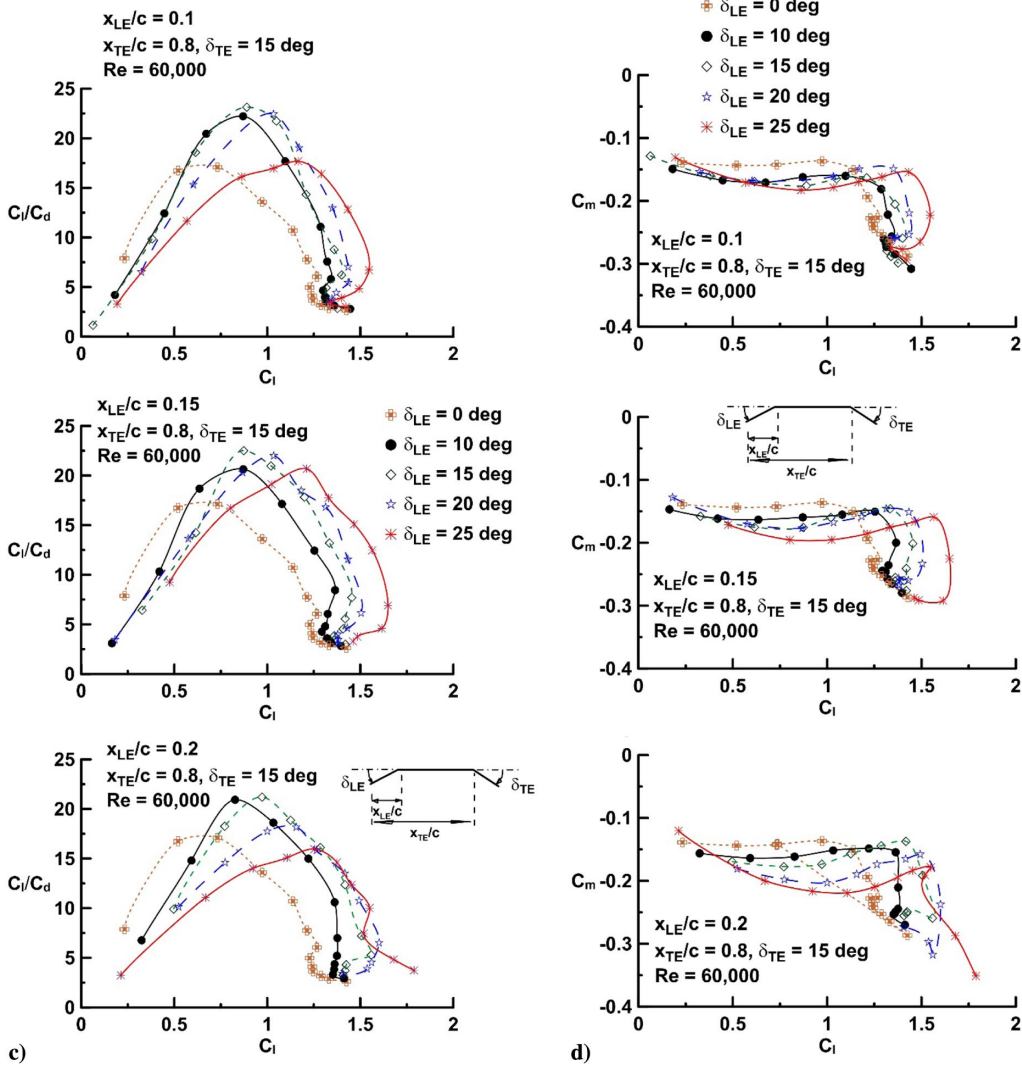


Fig. 4 (Continued).

would be linearly dependent on δ_{TE} , which is seen to be the case for $\delta_{TE} < 20^\circ$ deg. Higher flap settings may see a deviation from this linear dependency due to large-scale separation off the flap surface. The minimum drag coefficient displays a parabolic increase with δ_{TE} such that a marked increase in $C_{d\min}$ only occurs for flap angles of 15 and 20 deg (and thus contributes to the formation of a peak in C_l/C_d , the drag increase reducing the lift-to-drag ratio for the largest flap angle).

C. Leading and Trailing Edge Flaps

The length and setting angle of the LE flaps is examined in Fig. 4. In all cases the TE flap extent was 20% of the chord with a setting angle (δ_{TE}) of 15 deg. LE flaps are well-documented in their ability to delay stall [14]. They do this by attenuating the LE suction peak which reduces the adverse pressure gradient the leeward surface's boundary layer must negotiate. LE flaps have little impact on the fully attached flow lift coefficient, but do typically cause a small negative C_m increment (due to camber) and a small drag increment. These characteristics are consistent with the data shown in Fig. 4. Note that the $\delta_{LE} = 0^\circ$ deg case is included in all plots constituting Fig. 4 as a common point of reference. Deflecting the LE flap causes a moderate downward shift of the prestall lift curve, the shift increasing with the length of the flap (Fig. 4a). The downward shift of C_l appears fairly insensitive to the actual flap angle except for the largest chord flap, $x_{LE}/c = 0.2$. Increasing δ_{LE} causes a modest rise in $C_{l\max}$. The angle-of-attack range over which the lift curve is linear is reduced by the LE flaps (Fig. 4a). This is caused by downward flap rotation

promoting separation from the leading edge for negative α . This promotes a loss of C_l caused by the low-pressure zone of separation behind the flap's lower surface (as will be shown later).

LE flap rotation has a notable effect on the drag polar (Fig. 4b). The minimum drag coefficient is seen to increase, with a concomitant increase in $C_{l\text{md}}$ such that $C_{d\min}$ is almost coincident with the onset of airfoil stall. The net impact of the flaps is reflected in their efficiency, C_l/C_d (Fig. 4c). The maximum lift-to-drag ratio is increased significantly by LE flap deflection. Increasing δ_{LE} causes the peak efficiency to occur at a higher C_l . Most of the tested LE flap lengths provide performance improvement compared with the TE flap alone.

The quarter chord C_m (Fig. 4d) shows the greatest impact of the LE flap length. Rotating the flap downward systematically shifts the pitching moment curve negatively, a consequence of greater airfoil camber. Increasing the length of the flap amplifies this shift for a given δ_{LE} and creates a greater sensitivity to δ_{LE} .

The axial force that is developed by the airfoil is indicative of the ability of the LE flap to generate a forward-acting force component. This axial force may have two constituents: a LE suction develops as the airflow accelerates around the airfoil's nose from the windward stagnation point (and thus requires that the airfoil has thickness), and a camber thrust that originates from the pressure differential acting across forward sloping airfoil elements. LE suction is effectively zero for a thin sharp airfoil, but a camber thrust may be realized from a net positive force acting on a forward-facing flap element. For an airfoil, the attainable LE thrust may be expressed as

$$\eta = \frac{C_l \sin \alpha - (C_d - C_{d\min}) \cos \alpha}{C_l \sin \alpha} = 1 - \frac{(C_d - C_{d\min})}{C_l \tan \alpha} \quad (1)$$

The attainable LE thrust as defined by Eq. (1) is bounded at 0 as a lower limit and has a maximum of 1, indicating that full LE thrust on the flap is developed (with the assumption of inviscid flow, this implies that the forward-acting axial force component exactly cancels the aft acting component of the normal force). Figure 5 presents the calculated η as affected by the size and setting angle of the LE flap. Data are presented as a function of C_l (Fig. 5a) and α (Fig. 5b) to clarify η 's behavior as a function of lift loading and the corresponding airfoil inclination. Increasing δ_{LE} shows a systematic increase in the attainable thrust for a given α or C_l . The attainable thrust is a maximum at low angles of attack, where it will be shown that the flow is mostly attached over the LE flap. A comparison with Fig. 4c indicates that $(C_l/C_d)_{\max}$ is within the C_l range for each geometry at which η is generally close to 1. Consequently, peak efficiency occurs with smooth on-flow onto the flap (suggested by the high value of η). A similar result was reported for application of LE vortex flaps on a delta wing [26]. The effect of increasing the length of the LE flap is one of extending the α range over which significant forward-acting thrust is developed. In all instances, η initially shows a plateau and then a subsequent drop with increasing angle of attack that is likely

associated with the onset and progression of separation over the flap, or a lack of flow re-attachment on the flap. On delta wings [27] with LE vortex flaps, the attenuation of η with increasing angle of attack occurs due to the LE vortex expanding and migrating off the flap such that suction recovery is lost.

A summary of key aerodynamic parameters is presented in Fig. 6. The maximum lift coefficient is observed to have a weak parabolic dependence on δ_{LE} , progressively increasing with flap angle (Fig. 6a). Lengthening the flap (x_{LE}/c) increases $C_{l\max}$ moderately for a given δ_{LE} . Maximum aerodynamic efficiency, $(C_l/C_d)_{\max}$, also varies parabolically, with a peak evident at $\delta_{LE} \approx 15$ deg for all three flap lengths (e.g., rotating the $x_{LE}/c = 0.1$ flap to $\delta_{LE} = 15$ deg yields a 35% increase in peak lift-to-drag ratio compared with the TE flap alone, and a 106% increase compared with the flat plate; see Fig. 6b). Increasing the length of the LE flap reduces $(C_l/C_d)_{\max}$ moderately. The $x_{LE}/c = 0.1$, $\delta_{LE} = 15$ deg setting is optimal for the tested geometries in terms of the peak lift-to-drag ratio.

The angle of attack at which the maximum lift-to-drag ratio occurs relates to the incidence angle between the wing and fuselage that may be required for a flight vehicle to maximize range or glide slope (Fig. 6c). It may be preferable for the incidence angle to be set so as to lessen the fuselage contribution to drag at $(C_l/C_d)_{\max}$, or the orientation of the fuselage at other flight conditions. This $(\alpha_{(C_l/C_d)_{\max}})$ angle of attack (Fig. 6c) is seen to increase parabolically

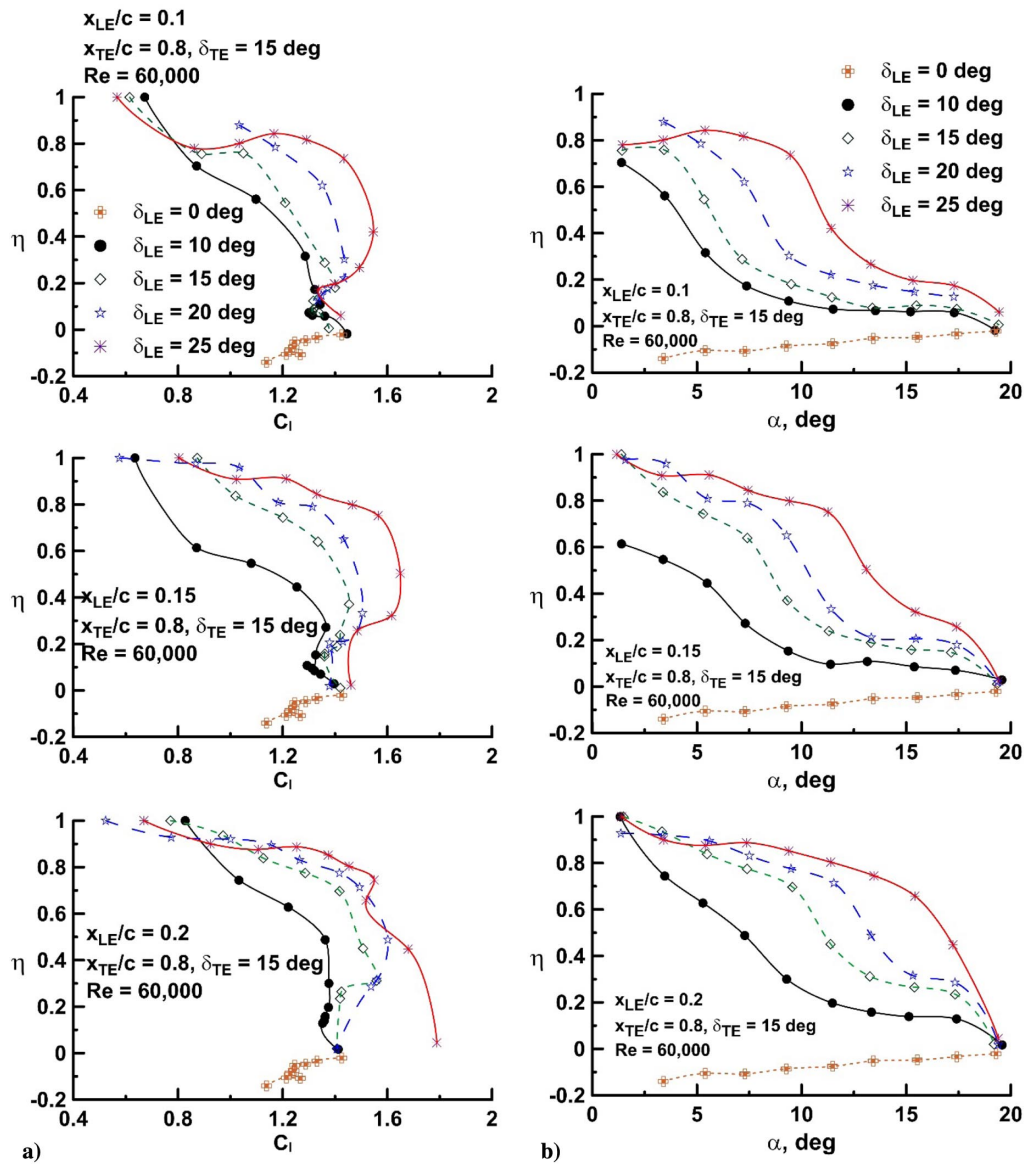


Fig. 5 Effect of δ_{LE} and flap length on the calculated attainable leading edge thrust as a function of a) lift coefficient and b) angle of attack.

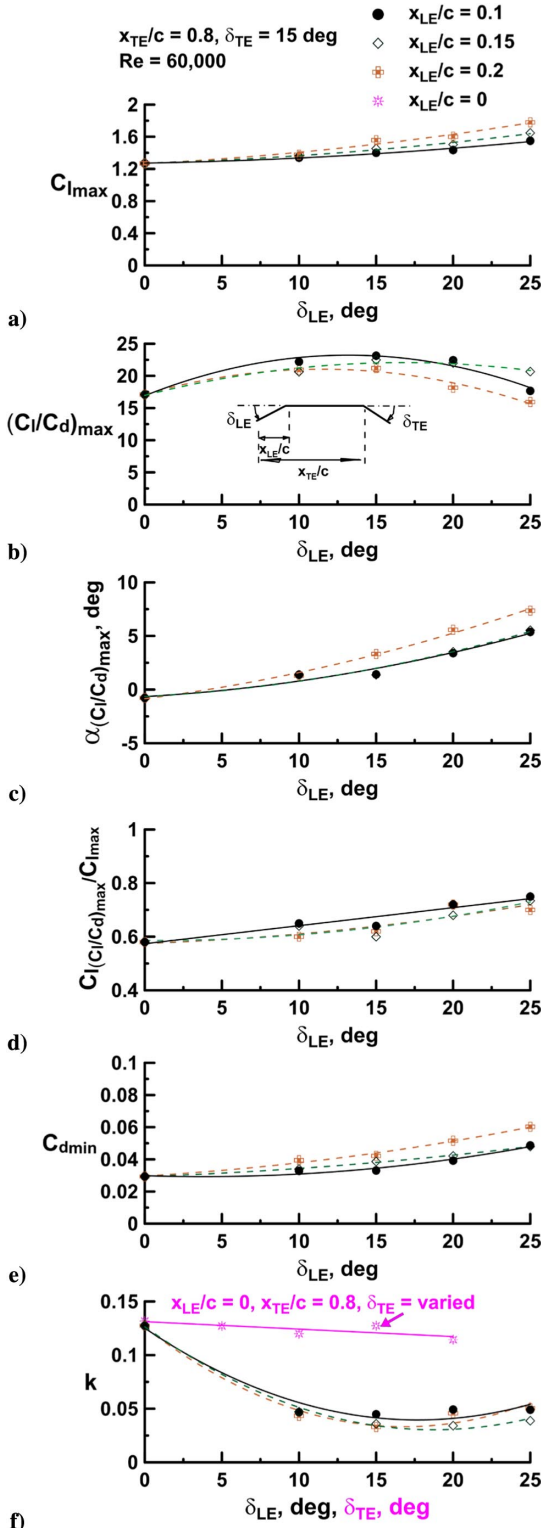


Fig. 6 Summary of salient aerodynamic parameters as affected by δ_{LE} : a) $C_{l\max}$, b) $(C_l/C_d)_{\max}$, c) $\alpha^*(C_l/C_d)_{\max}$, d) $C_l(C_l/C_d)_{\max}/C_{l\max}$, e) $C_{d\min}$, and f) k .

with LE flap angle, such that (assuming a level fuselage is desired) the incidence angle would vary from approximately 0 deg for no LE flap to ≈ 6 deg for $\delta_{LE} = 25$ deg. Consequently, how close the corresponding C_l for $(C_l/C_d)_{\max}$ is to stall is of interest. This is reflective of the margin before stall that the flight vehicle may have if flying to maximize range and encountered a gust. Figure 4 may also be used for reference. As shown in Fig. 6d, increasing the LE flap angle causes the value of C_l for $(C_l/C_d)_{\max}$ to increase from 58% to approximately 75% of $C_{l\max}$.

The minimum drag coefficient also increases parabolically with δ_{LE} (Fig. 6e). To quantify, for a 10% LE flap, $x_{LE}/c = 0.1$, rotating the flap from 0 to 25 deg results in a 63% increase in $C_{d\min}$. For the optimal case ($\delta_{LE} = 15$ deg), the penalty is 12.6%. Intuitively, lengthening the flap also causes a greater drag penalty for a given δ_{LE} .

Characterization of the effect of flap setting angle on the variation of drag due to lift provides insight into the pressure drag behavior. The drag polar for a cambered airfoil may be expressed as (the vertex form of a parabola)

$$C_d = C_{d\min} + k(C_l - C_{l\min})^2 \quad (2)$$

Here, the coefficient k relates to the curvature of the drag polar. The smaller the value of k , the lower the curvature of the function [Eq. (2)] with the implication of reduced pressure drag due to lift. The value of k is determined from linearization of the drag polar where C_d is plotted as a function of $(C_l - C_{l\min})^2$. Fitting a linear regression to the linear extent of the resulting plot then yields k . For polars that are not “well-behaved” (i.e., show some dispersion around a linear regression curve fit), a linearizing approach can sometimes be problematic. An alternative method to establish k that is more tolerant is directly using (it is still assumed that the drag polar has an essentially parabolic form):

$$C_d = aC_l^2 + bC_l + c \quad (3)$$

Equation (3) can readily be fitted to experimental data; the complication is in the interpretation of the terms. Drag due to lift (pressure as well as vortex—if a wing) has a lift coefficient squared dependency; however, C_d does not have a component that is proportional to C_l . Expanding Eq. (2) and comparing terms with Eq. (3) shows that

$$\begin{aligned} k &= a, & C_{l\min} &= -b/(2a) \\ \text{and } C_{d\min} &= c - kC_{l\min}^2 = c - b^2/(4a) \end{aligned} \quad (4)$$

where $C_{l\min}$ comes from determining the minimum in Eq. (3). Consequently, curve fitting the drag polar using a parabolic function yields the coefficients in Eq. (3), from which Eq. (2) can be established using Eq. (4).

Results of this procedure (to find k) are shown in Fig. 6f. The linearized polar approach and Eqs. (3) and (4) were used to find k ; both methods showed close accord. Two data sets are presented: one for the effect of deflection of the TE flap with $\delta_{LE} = 0$ deg (shown in pink) and the other for the effect of LE flap deflection with $x_{TE}/c = 0.8, \delta_{TE} = 15$ deg. The value of k ($= 0.13$) for $x_{LE}/c = 0$, $x_{TE}/c = 0.8, \delta_{TE} = 0$ deg is that of the flat plate. The drag due to lift dependency, k , shows a weak linear reduction with increasing δ_{TE} for the range examined. The effect of the LE flap deployment appears to saturate rapidly such that the variation of the drag due to lift (k) is relatively constant (a weak minimum is visible for $15 \leq \delta_{LE} \leq 20$) for the range of δ_{LE} tested. The drag due to lift is approximately 67% lower when an LE flap is deployed; average $k = 0.043$ compared with 0.13 for the flat plate. This is consistent with the data in Fig. 5, where the C_l domain over which η is elevated is coincident with the C_l range used to define k (as it corresponds to the region over which the “linearized” drag polar is linear and is well-represented by a parabolic curve fit). It is interesting that the value of k for the flat plate is close to those for the flat plates with the TE flap only; yet significant performance improvements are observed with a TE flap (see Fig. 3c). The C_l/C_d increase follows from the TE flaps shifting the drag polar to the right such that $C_{l\min}$ increases.

The drag reduction mechanism of the LE and TE flaps is different. The TE flaps reduce the drag coefficient by augmenting C_l . Thus, for a given lift coefficient, the angle of attack of the airfoil is reduced such that the aft component of the normal force is less [20,21]. The LE flaps reduce drag as a consequence of their geometric orientation in concert with the net loading across the flap [17]. Downward LE flap deflection yields a forward-acting force component that opposes drag. As long as the orientation of the LE flap is such that it has a

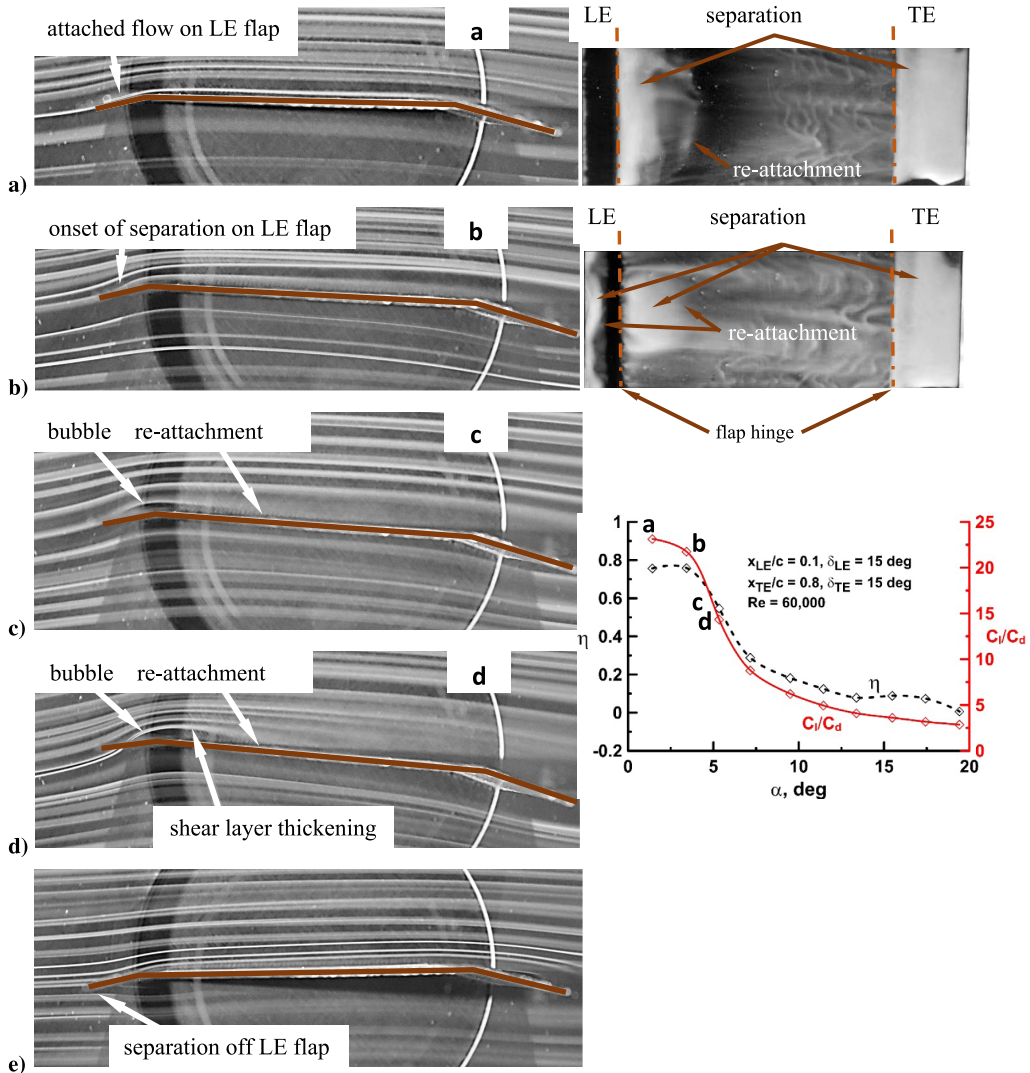


Fig. 7 Smoke and oil flow visualization over $x_{LE}/c = 0.1$, $x_{TE}/c = 0.8$, $\delta_{LE} = \delta_{TE} = 15$ deg for $\alpha =$ a) 1.5, b) 3, c) 4, d) 5, and e) -1 deg, $Re = 60,000$. Flow is left to right. Letters on inset plot correlate with streamline images.

forward-facing area and is producing a positive lift component, drag will lessen.

1. Flow Visualization

Figure 7 shows smoke rendering of streamlines as well as surface skin friction patterns around the $x_{LE}/c = 0.1$, $x_{TE}/c = 0.8$, $\delta_{TE} = \delta_{LE} = 15$ deg geometry. The location of the airfoil edge is shown as a brown line. Also included with the images is a plot showing both the attainable thrust and the lift-to-drag ratio, both presented as a function of α to aid in association with the flow visualization. Smooth on-flow onto the LE flap without separation (Fig. 7a) correlates with both high thrust and peak lift-to-drag ratio. The skin friction patterns also indicate attached flow on the LE flap with separation from the LE flap hinge line, forming a closed separation bubble. The TE flap hinge line is also seen to be a separation line such that flow over the TE flap is not fully attached. Increasing the angle of attack to 3 deg (Fig. 7b) shows localized separation on the LE flap with subsequent separation from the LE flap hinge line as seen for $\alpha = 1.5$ deg.

The precipitous drop in both η and C_l/C_d for $\alpha \geq 4$ deg (Figs. 7c and 7d) is strongly coupled, and is seen to associate with separated flow over the LE flap with subsequent re-attachment downstream forming a long bubble. Increasing α from 4 to 5 deg does not appear to increase the length of the bubble, but its height above the surface ($\approx 3\%$ of the chord). Setting the airfoil at a small negative angle of

attack (-1 deg; Fig. 7e) shows separation off the LE lower surface that contributes to the loss of lift seen in Fig. 4a for $\alpha < 0$ deg.

The net result is that peak C_l/C_d correlates with smooth on-flow onto the LE flap with no separation over the flap, a flow condition reflected in high attainable LE thrust. Localized separation over the flap superseded by larger-scale separation with attachment downstream of the flap in the form of a long bubble is seen with increasing α beyond that required for $(C_l/C_d)_{max}$.

2. Surface Pressure Measurement

Figures 8a–8c present surface pressures measured over the $x_{LE}/c = 0.1$, $x_{TE}/c = 0.8$, $\delta_{TE} = \delta_{LE} = 15$ deg geometry (i.e., optimal) and the flat plate. Also included in the figures are lift and drag coefficients obtained through integration of the surface pressures (Figs. 8d–8g).

Deflecting the LE and TE flaps causes suction over the forward region of the airfoil's upper surface to increase systematically with α ($\alpha \leq 4$ deg) (Fig. 8b). Suction peaks are seen in the vicinity of the flap hinges at 10 and 80% of the chord as is typical for a plain flap. Over the LE flap for $\alpha = 2$ to 6 deg, a small plateau is evident in the C_p trace (Fig. 8b), which suggests localized separation as shown in surface skin friction renderings (Fig. 7b). Peak suction levels (Fig. 8b) are far higher than on the flat plate (Fig. 8c) due to the camber addition caused by the TE flap. The upper surface C_p traces for $\alpha > 6$ deg (Fig. 8b) resemble those for the flat plate (Fig. 8c) and

imply large-scale separation on the upper surface. The upper surface of the flapped airfoil generates net suction even at an α at which C_l is negative ($\alpha = -6$ deg). Comparing Figs. 8a and 8b shows that the suction on the lower surface outweighs the suction on the upper surface. This differential explains the rapid loss of C_l compared with the TE flap alone for negative α (see Fig. 4a).

For a given positive α , compression on the lower surface aft of the LE flap is enhanced toward the front of the airfoil compared with the flat plate (Figs. 8a and 8c). Over the TE flap's length, a rapid acceleration of the flow on its lower surface is observed (see Fig. 8a). Figure 7e indicated flow separation from the lower lip of the LE flap at negative α . This observation is supported by the lower surface pressure traces, where a plateau exists extending from the LE aft, until flow reattachment is suggested by pressure recovery (Fig. 8a). The chordwise extent of the plateau increases with negative angle of attack.

The upper surface C_p 's over the flat plate show a distinct suction peak only for $\alpha = 2$ deg (Fig. 8c). For $\alpha > 2$ deg, suction over the forward length of the upper surface of this airfoil presents as a broad plateau (which is consistent with the presence of a large bubble extending from the LE [15,17]) and for $\alpha > 8$ deg shows uniform loading with negligible pressure recovery toward the TE, indicative of large-scale separation (Fig. 8c).

The upper and lower surface lift coefficient components acting on the two airfoils are shown in Fig. 8d, calculated through integration of the surface pressures. For both airfoils, for $\alpha > 5$ deg, each surface carries an essentially constant portion of the loading: $\approx 78\%$ (upper)

and $\approx 22\%$ (lower) for the flapped airfoil and $\approx 95\%$ (upper) and $\approx 5\%$ (lower) for the flat plate. Consequently, the lower surface of a flat plate contributes negligibly to the production of lift. For lower angles of attack, the upper surface is seen to contribute an increasingly larger proportion of the net lift.

The lift load carried by the LE and TE flap as well as the central panel are examined in Fig. 8e. Also included are the total C_l calculated from pressure integration and that from force balance measurement. As seen, agreement between the force balance data and that from pressure measurement is excellent. The lift contribution of both the LE and TE flap extents is approximately constant and is weakly dependent on α . The central panel, representing 70% of the lifting area, provides the loading associated with the α dependency of the lift curve.

The contribution of the LE, TE, and central panel to the pressure drag coefficient is explored in Figs. 8f and 8g. The data are presented as a function of α (Fig. 8f) and C_l (Fig. 8g) to aid in interpretation. The pressure drag ($C_d - C_{d\min}$) from force balance measurement is also included in the figures and shows close accord with the drag estimate from pressure integration, especially in the prestall regime ($\alpha < 10$ deg). The drag contribution of the TE flap is quite constant, whereas that of the LE flap is negative, indicating a forward-acting thrust. The thrust is seen to peak at approximately $\alpha = 3$ deg ($C_l \approx 1.1$), a value close to that at which $(C_l/C_d)_{\max}$ is achieved (see Fig. 4c). Parallel orientation of the LE flap with the freestream ($\alpha = 15$ deg, $C_l \approx 1.35$) marks the divider where the LE flap

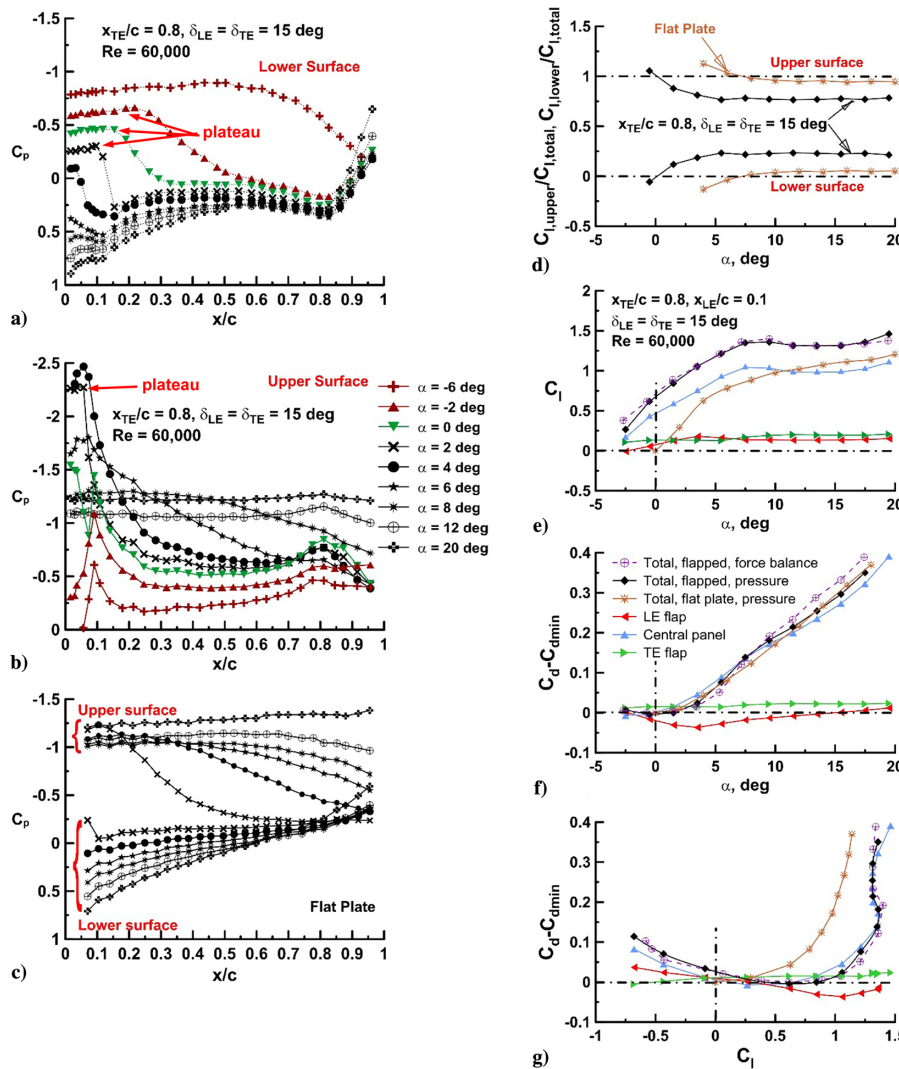


Fig. 8 Measured pressure coefficient for the optimal flapped airfoil a) lower surface, b) upper surface, and c) the flat plate as well as integrated d) lift components, e) lift coefficient, and f,g) drag coefficient.

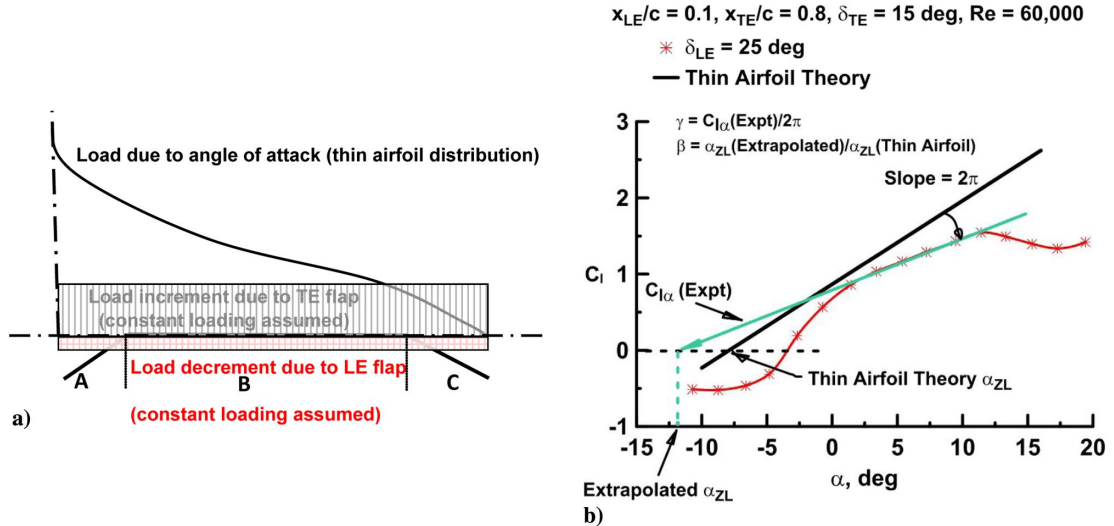
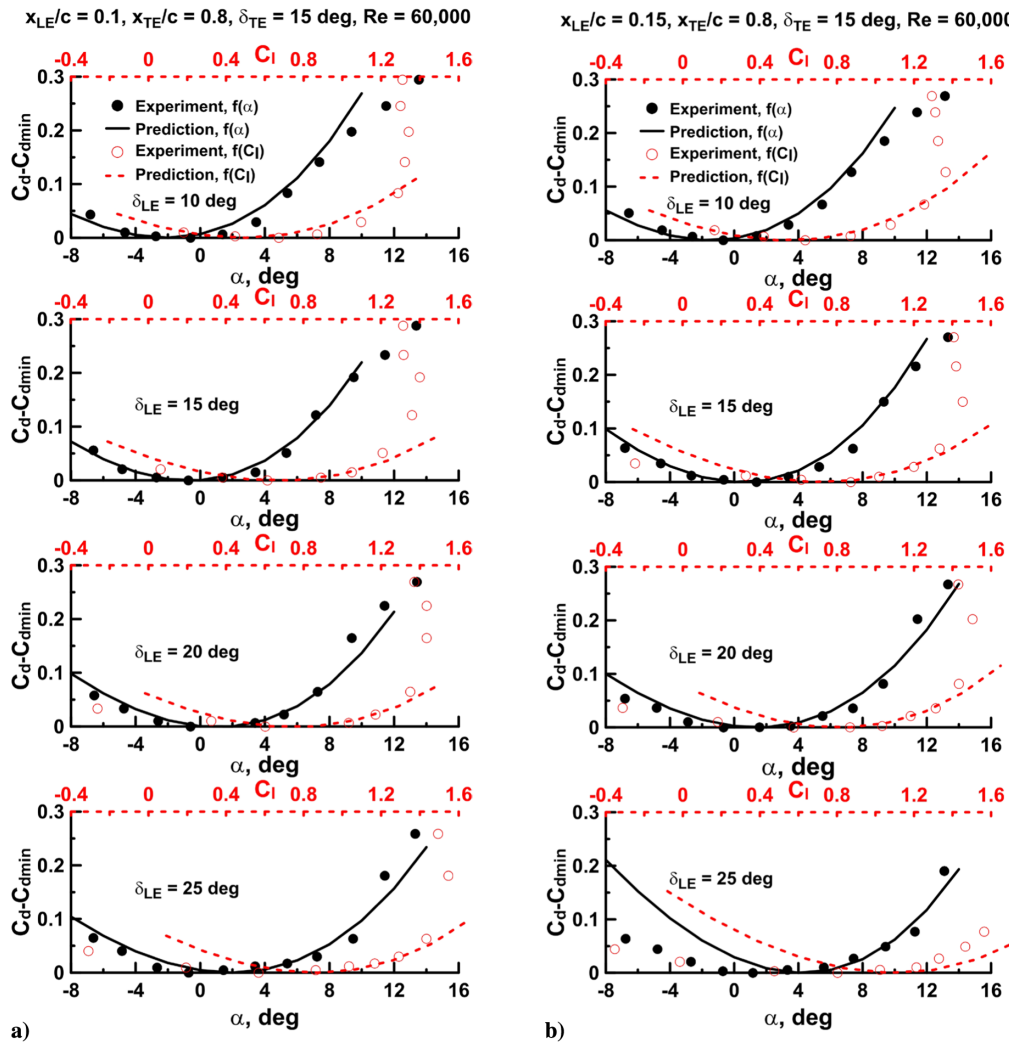


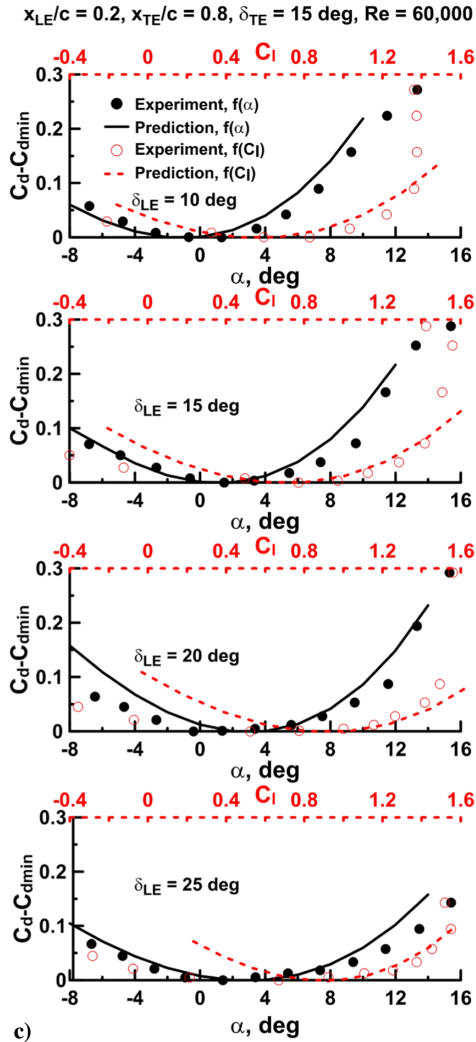
Fig. 9 Semi-empirical a) prescribed chordwise loading and b) lift corrections.

transitions from providing thrust to contributing to drag (Fig. 8f). As a function of α , the drag due to lift of the flat plate is close to that of the flapped airfoil (Fig. 8f). However, the lift augmentation of the TE flap causes a significant reduction in the required angle of attack for a given C_l , such that the drag of the flapped airfoil is far lower than the flat plate when examined as a function of C_l (Fig. 8g).

Fig. 10 Comparison of theory and experiment for x_{LE}/c = a) 0.1, b) 0.15, and c) 0.2.

D. Analytic Estimation of the Drag Coefficient

Prediction of the effect of the LE and TE flaps on the drag coefficient would be valuable not just for performance estimation, but also as a tool to characterize the effect of the flaps. Considering the geometry of the flat plate airfoils, an analysis based on thin airfoil theory would be appropriate. Following thin airfoil



theory [22,23,25], the following variable transformations are defined:

$$x/c = 0.5(1 - \cos \theta), \quad \theta = \cos^{-1}(1 - 2x/c) \quad (5)$$

The sectional lift coefficient is given by [23]

$$C_l = 2\pi \left(\alpha + \frac{1}{\pi} \int_0^\pi \frac{dz}{dx} (\cos \theta - 1) d\theta \right) \quad (6)$$

Note that the slope of the LE flap is δ_{LE} and that of the TE flap is δ_{TE} . Substituting the flap angles into Eq. (6) with the appropriate limits gives

$$C_l = 2\pi \left(\alpha + \frac{1}{\pi} \int_0^{\theta_{LE}} \delta_{LE} (\cos \theta - 1) d\theta + 0 - \frac{1}{\pi} \int_{\theta_{TE}}^\pi \delta_{TE} (\cos \theta - 1) d\theta \right) \quad (7)$$

where the slope of the central section between the flaps is zero as depicted in Fig. 1 and the signs are adjusted such that downward LE and TE flap deflection is positive. Evaluation of Eq. (7) yields

$$C_l = 2\pi \left(\alpha + \frac{\delta_{LE}}{\pi} (\sin \theta_{LE} - \theta_{LE}) + \frac{\delta_{TE}}{\pi} (\pi + \sin \theta_{TE} - \theta_{TE}) \right) \quad (8)$$

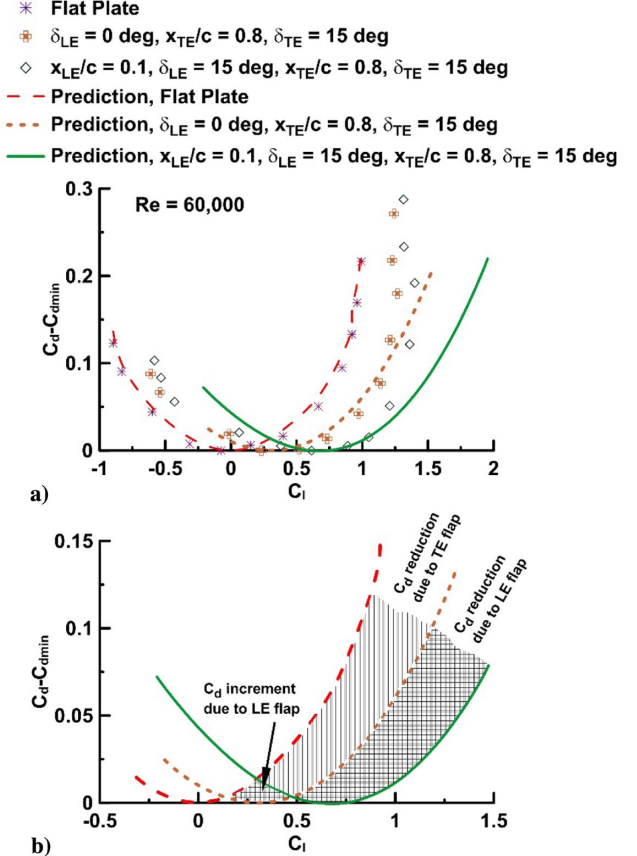


Fig. 11 Drag contribution of a) the leading and trailing edge flaps and b) drag break down.

where the terms in braces are the contribution of a planar flat plate (angle of attack), LE flap, and TE flap to the lift coefficient. The total lift is simply the linear addition of the components. Equation (8) is inviscid in formulation. It would not be expected that this expression would be representative for the flows under consideration without modification. To be consistent with a simple analytic analysis, the chordwise distribution of the loading for each component (i.e., due to α and the LE and TE flap) will be prescribed. The airfoils under consideration will generally experience some extent of separation that would alleviate the large adverse pressure gradient predicted by thin airfoil theory. Separation generally implies chordwise extents of flow with negligible pressure gradient [9,17]. It will be assumed that the chordwise loading due to angle of attack will have the load distribution given by thin airfoil theory, but the contributions of the LE and TE flaps will be uniformly distributed over the chord (see Fig. 9a). Although this is a simplification, moderate deflection of a TE flap does give a fairly uniform increase in upper surface loading [28]. Viscous effects (separation) would not only re-organize the loading experienced by the airfoil, but also alter the loads. Referring to Eq. (8), this would have two contributors: a reduction of the lift curve slope ($2\pi/\text{rad}$) and shift of the zero-angle-of-attack lift coefficient (a camber effect caused by the LE and TE flaps). The inviscid zero-angle-of-attack lift coefficient follows from Eq. (8) as

$$C_{l0} = 2\delta_{LE}(\sin \theta_{LE} - \theta_{LE}) + 2\delta_{TE}(\pi + \sin \theta_{TE} - \theta_{TE}) \quad (9)$$

with a corresponding $\alpha_{ZL} = -C_{l0}/C_{la}$. To estimate the lift coefficient, the experimental value of C_{l0} could be used directly; however, most theory [23,25] defines C_l as a function of lift curve slope and α_{ZL} . Thus, for consistency a similar approach will be used. Figure 9b shows that correcting C_{l0} requires a modification to both the lift curve slope and α_{ZL} , defined as γ and β in the image such that

$$\gamma = C_{la}(\text{Expt})/2\pi, \quad \beta = \alpha_{ZL}(\text{Extrapolated})/(-C_{l0}/(2\pi)) \quad (10)$$

where "Extrapolated" refers to extrapolation of the linear portion of the experimental lift curve until $C_l = 0$; C_{l0} in Eq. (10) is given by Eq. (9). C_{la} (Expt) is the lift curve slope calculated over the linear extent of the experimental data. The chordwise load distribution given by thin airfoil theory is $\propto (1 + \cos \theta)/\sin \theta$ [23,25]. Integration of this distribution along the chord to an arbitrary location allows determination of the load developed (specifically the lift curve slope per unit length) from the LE to that point and is given by:

$$C_{la}(\theta) = 2(\theta + \sin \theta) \quad (11)$$

Evaluating Eq. (11) at the TE ($x/c = 1, \theta = \pi$) yields 2π , while setting $x/c = 0.5 [\theta = \pi/2, \text{from Eq. (5)}]$ gives $C_{la} = 5.142$; that is, 81.8% of the total lift (for a given α) of the airfoil is developed over the forward half of the chord. Equations (9–11) facilitate the estimation of the loading (caused by the flaps and α) over the LE flap, central panel, and TE flap extents, designated as regions A, B, and C in Fig. 9a, respectively. Thus (noting that $C_l = C_{IA} + C_{IB} + C_{IC}$)

$$\begin{aligned} C_{IA} &= (x_{LE}/c)\gamma\beta C_{l0} + 2\pi\gamma\alpha(C_{la}(\theta_{LE})/2\pi) \\ C_{IB} &= (x_{TE}/c - x_{LE}/c)\gamma\beta C_{l0} + 2\pi\gamma\alpha([C_{la}(\theta_{TE}) - C_{la}(\theta_{LE})]/2\pi) \\ C_{IC} &= \underbrace{(1 - x_{TE}/c)\gamma\beta C_{l0}}_{\text{LE+TE flap loading}} + \underbrace{2\pi\gamma\alpha([2\pi - C_{la}(\theta_{TE})]/2\pi)}_{\text{loading due to } \alpha} \end{aligned} \quad (12)$$

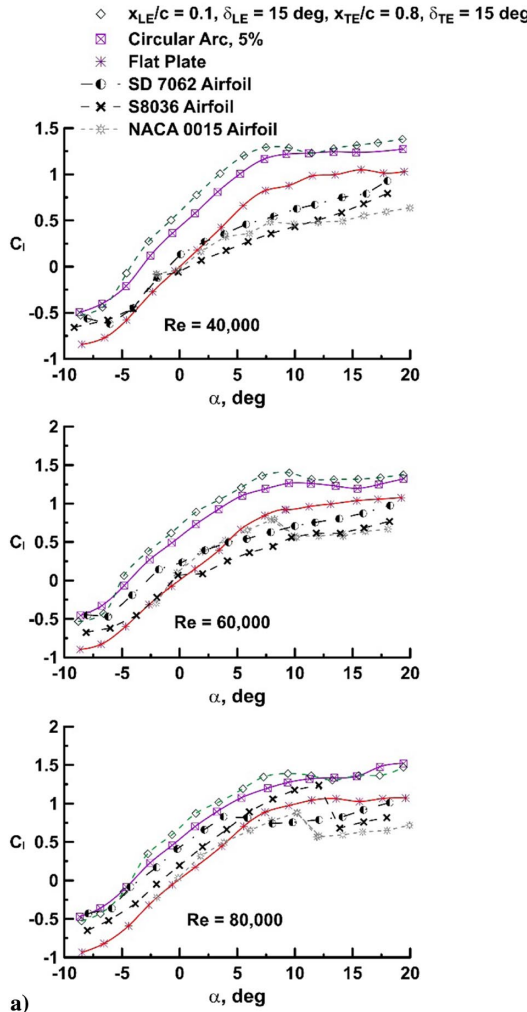


Fig. 12 Comparison of flat plate and conventional airfoils: a) lift, b), drag, c) lift-to-drag ratio, and d) pitching moment coefficient.

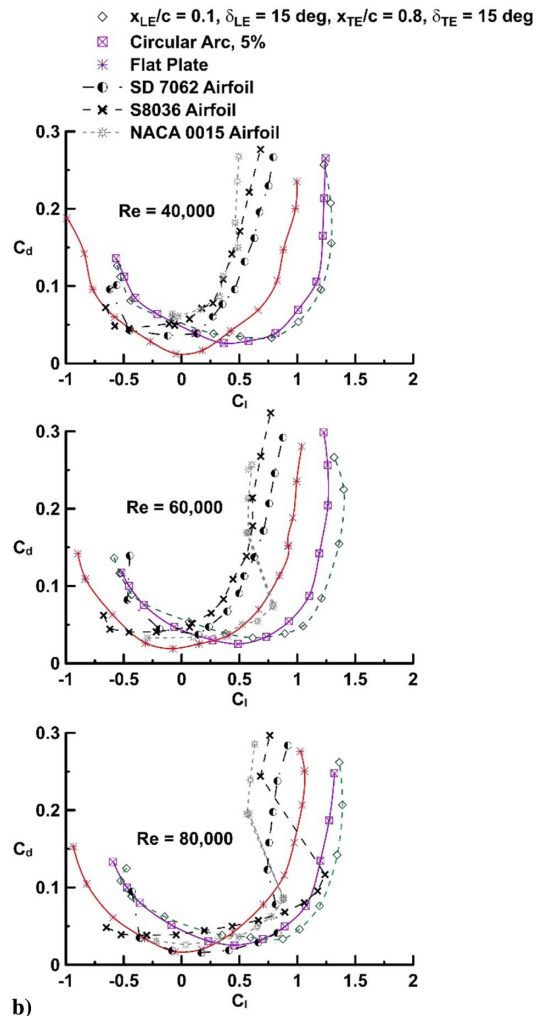
Equations (12) incorporate the viscous corrections to the lift curve slope and α_{ZL} given by Eq. (10). The lift coefficient at $\alpha = 0$ deg is calculated using Eq. (9). The drag due to lift coefficient can now be established from the components of the loading in the freestream direction.

$$C_d = -C_{IA} \tan(\delta_{LE} - \alpha) + C_{IB} \tan(\alpha) + C_{IC} \tan(\delta_{TE} + \alpha) \quad (13)$$

Comparison of Eq. (13) with the current experimental data showed a slight overprediction of drag. Inclusion of the LE suction that would have been developed was observed to improve agreement. This approach has precedent for thin sharp wings as long as flow reattachment occurs after separation as embodied in Polhamus's LE suction analogy [29]. The LE suction is assumed to be recovered as a force normal to the LE flap (i.e., vortex lift). Inclusion of this vortex lift component has improved correlation between theory and experiment for flat plate rectangular wings [30]. Using an equation for the LE suction from Ref. [31] gives a final expression for the drag due to lift coefficient of the flapped airfoil as:

$$\begin{aligned} C_d &= -C_{IA} \tan(\delta_{LE} - \alpha) + C_{IB} \tan(\alpha) + C_{IC} \tan(\delta_{TE} + \alpha) \\ &\quad - 2\pi\alpha^2\gamma \tan(\delta_{LE} - \alpha) \end{aligned} \quad (14)$$

Evaluation of Eq. (14) gives $C_d > 0$ for all α . Thus, to afford comparison with experiment it is necessary to evaluate Eq. (14) to generate a drag polar for the desired geometry. The minimum drag coefficient of the resulting polar should then be determined and subtracted off Eq. (14) to yield $C_d - C_{d\min}$, which can then be compared with experiment.



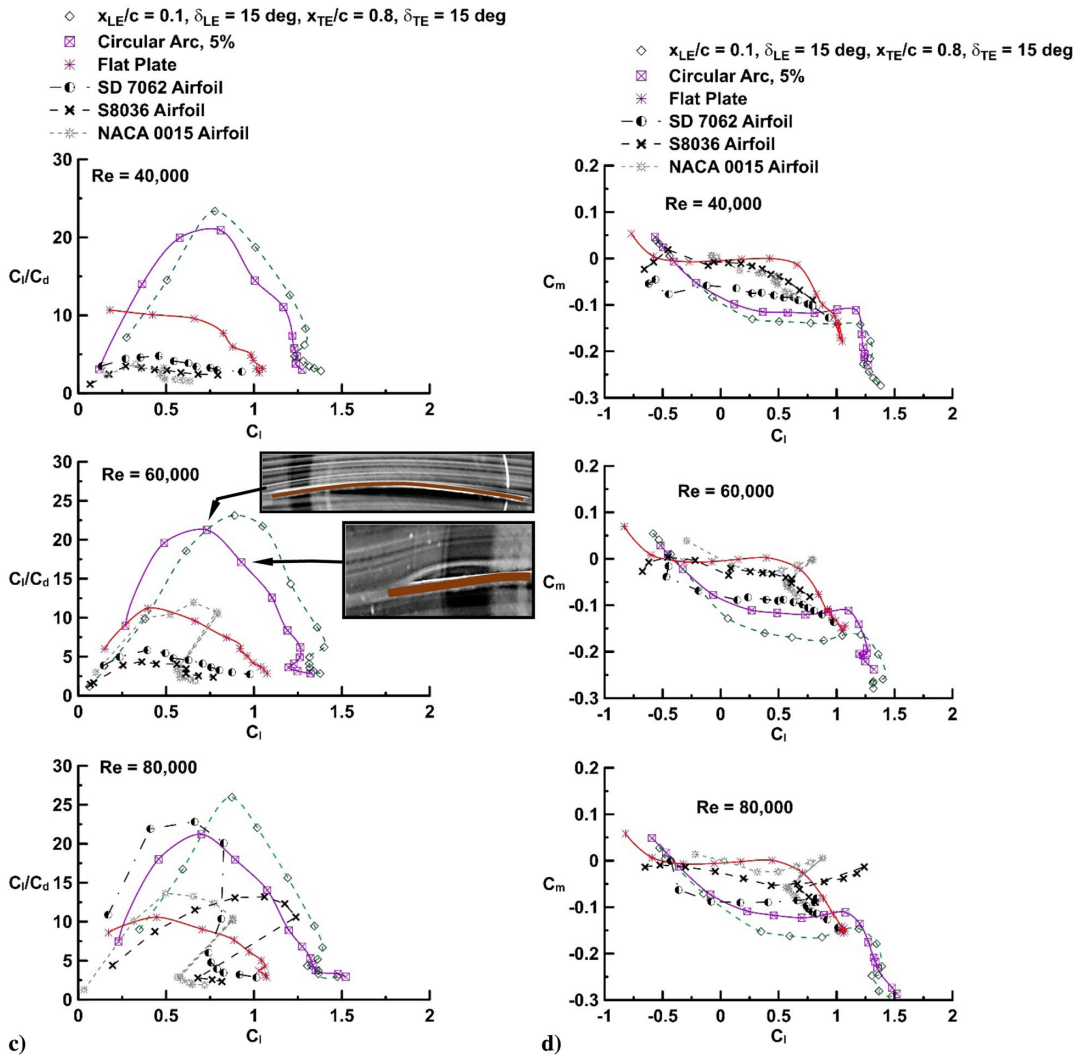


Fig. 12 (Continued).

Referring to Fig. 9b, drag estimates would only be expected to be representative within the linear extent of the lift curve (and the corresponding α range) as used to define Eq. (10). Figure 10 shows comparisons of Eq. (14) against the current experimental data. The drag coefficient is presented as a function of both α [solid axis—as Eq. (14)'s formulation is a function of angle of attack] and C_L [dashed axis—relevant from a flight perspective] for each LE flap setting (see Fig. 10). The agreement of theory and experiment is very good in the “linear” range of the C_L curve, ≈ 0 to 12 deg α —especially considering the complexity of the flows that are being modeled. The $C_d - C_{d\min}$ behavior as a function of δ_{LE} and x_{LE}/c is well-captured and supports the prescribed load distributions in Eq. (12). Note that, if evaluating a planar flat plate, β would be singular ($C_{l0} = 0$); for this case, $C_d - C_{d\min} = C_l \tan \alpha$.

Equation (14) can be used to evaluate the contribution of the LE and TE flap to the drag experienced by the airfoil. Figure 11a presents the drag due to lift of the flat plate, 15 deg TE flap and optimal case, $x_{LE}/c = 0.1, x_{TE}/c = 0.8, \delta_{LE} = \delta_{TE} = 15$ deg. Also included are predictions using Eq. (14); the theoretical estimates are representative of experiment (as also seen in Fig. 10) and predict the lift coefficient for $C_{d\min}$ well (Fig. 11a). Consequently, Eq. (14) can be used to decompose the drag constituents associated with flap deflection, as shown in Fig. 11b. Deflecting the TE flap down causes a significant drag reduction compared with the flat plate, stemming from the reduced α for a given C_l . The LE flap causes a drag increment compared with the TE flap alone at low lift coefficients for which $\alpha < -1.7$ deg ($C_l \approx 0.5$). However, the LE flap provides an

additional drag reduction compared with the TE flap alone for $C_l > 0.5$, which corresponds to $\alpha > -1.7$ deg. For negative α , such that $C_{lA} < 0$, Eq. (13) predicts a significant drag contribution caused by the LE flap [as C_{lA} is negative, in conjunction with $\tan(\delta_{LE} - \alpha)$ gives a large drag contribution, whereas for the TE flap alone, $\delta_{LE} = 0$ deg, reducing the drag component relative to $\delta_{LE} > 0$ deg]. Increasing the inclination of the LE flap causes a greater drag reduction (not shown) that would (in application) be offset by the accompanying increase in $C_{d\min}$. Overall, the TE flap (for the geometries tested) provides the greatest drag reduction, whereas the LE flap compounds the drag reduction, but only for α greater than approximately 0 deg.

E. Conventional and Cambered Flat Plate Airfoils

The data indicate that significant performance enhancements are achievable compared with a thin flat plate, using a TE flap alone, or in conjunction with a LE flap. Also of interest is the performance of the optimal LE and TE flap combination compared with a thin circular arc section as well as three “conventional” reference airfoils. The circular arc airfoil has been found to perform well at $Re < 100,000$, with a camber of approximately 5% cited as optimal [13,16]. Reference airfoils include two low-Reynolds-number profiles: the S8036 and the SD 7062. Additionally, although the NACA 0015 is a turbulent-flow profile and is thus not necessarily well-suited for low- Re use, its ubiquitous application suggests that its inclusion should be of value.

Figure 12 presents a comparison of the three airfoils: optimal flapped ($x_{LE}/c = 0.1$, $\delta_{LE} = \delta_{TE} = 15$ deg and $x_{TE}/c = 0.8$) and the circular arc section. The flat plate is included in all figures as a point of reference. Tests were undertaken at $Re = 40,000$, 60,000, and 80,000, a range spanning common MAV operation. At $Re = 40,000$, all three conventional airfoils show performance indicative of laminar separation (Figs. 12a and 12b): the absence of a C_l/\max peak (which is requisite upon the formation of a LSB at low Re , to serve as the boundary-layer transition mechanism), a distinct $C_{l\alpha}$ break for $\alpha > 0$ deg, and a rapid C_d rise (Fig. 12b). Increasing Re generally shows an improvement in the airfoil characteristics (marked for $Re = 80,000$) although performance is inferior to the cambered flat plates. As an example, an increase of Re from 40,000 to 80,000 causes the lift-to-drag ratio to rise by 260, 376, and 279%, whereas $C_{d\min}$ drops 57, 56, and 15% for the NACA 0015, SD 7062, and S8036 airfoils, respectively.

Efficiency of the 5% camber circular arc profile is close to that of the optimal flapped flat plate geometry although the peak (C_l/C_d)_{max} is lower (10.6, 8.1, and 18% less than the flapped plate, for

$Re = 40,000$, 60,000, and 80,000, respectively; Fig. 12c). The inset image displaying streamlines over the circular arc at the (C_l/C_d)_{max} condition shows attached flow over the airfoil, a similar result to that seen for the optimal flapped geometry (Fig. 7a). The formation of a small LE separation bubble on the circular arc airfoil (the inset image is zoomed into the LE) is coincident with a reduction in the lift-to-drag ratio at $C_l = 0.9$.

The thin plate airfoils show less C_m sensitivity to Re than the conventional airfoils (Fig. 12d). The significant amount of camber of the circular arc and flapped plate causes a substantial nose down pitching moment. The higher effective camber of the flapped plate compared with the circular arc is reflected in both larger α_{ZL} values as well as stronger nose down pitching moments.

The overarching result conveyed within Fig. 12 is that the thin plates have low Re sensitivity, whereas that of the conventional airfoils is profound. Additionally, a simple flat plate with an appropriately sized and deflected LE and TE flap can yield meaningful performance improvements compared with a circular arc airfoil with an average increase in the maximum lift-to-drag ratio of

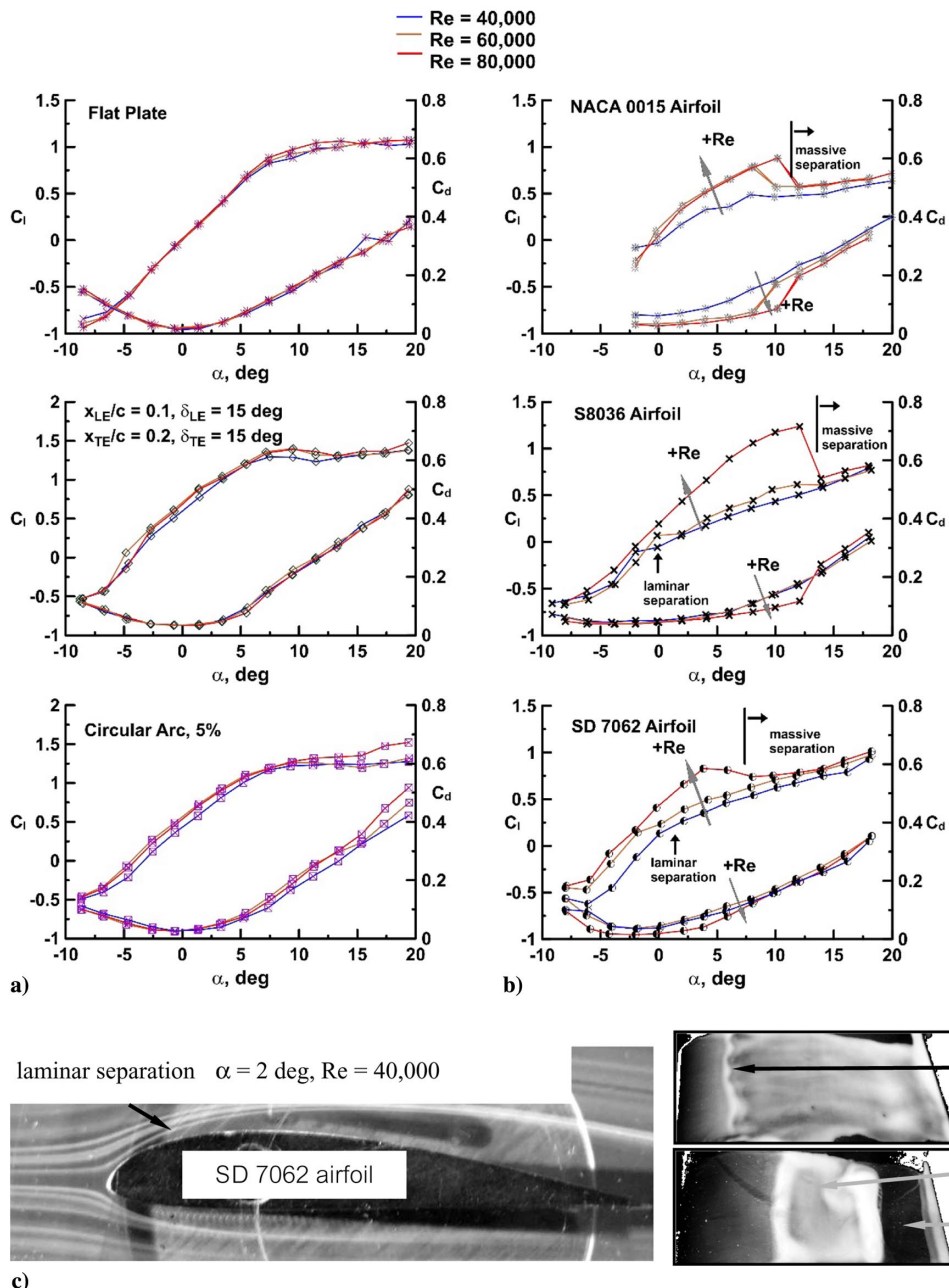


Fig. 13 Reynolds number sensitivity of a) flat plates and b) conventional airfoils. Flow visualization c) showing laminar separation and LSB formation over the SD 7062 airfoil (flow is left to right).

14% for all of the three Reynolds numbers considered. The conventional airfoils themselves also have highly disparate performance; while all perform poorly at $Re = 40,000$, their behavior does not improve consistently with Re . Only the SD 7062 shows an improvement sufficiently significant at $Re = 80,000$ so as to be competitive with the cambered plates.

Reynolds number sensitivity is examined directly in Fig. 13 for each airfoil over the tested Re range. The lift curves are associated with the left-hand-side axis, whereas the drag curves (lower set of plots in each graph) are associated with the right-hand-side axis. The flat plate shows a notable insensitivity to Re for the range tested. This implies that the shear layer behavior is such that transition and flow reattachment occur at a similar location for a given α for each tested Re number. The flapped flat plate and circular arc section show a slight sensitivity to Re with a small improvement in lifting performance for $Re > 40,000$ (Fig. 13a).

Figure 13b shows the sensitivity of the conventional airfoil geometries to Re . The NACA 0015 shows laminar separation without transition at $Re = 40,000$. An increase in Re to 60,000 shows the formation of a $C_{l\max}$ peak as well as a concomitant C_d rise in the drag polar, both indicative of the presence of a LSB and the onset of "conventional" TE stall. Note that massive separation shows a coalescence of data for all three Reynolds numbers; once large-scale separation is present, the Reynolds number has little effect on the lift and drag coefficients. A consistent behavior is also seen for the S8036 and SD 7062 airfoil in terms of massive separation causing an amalgamation of C_l (and C_d) for the three Reynolds numbers, for a given α .

Both the S8036 and SD 7062 profiles display laminar separation for $\alpha > 0$ deg at $Re = 40,000$ and 60,000, suggested by a marked C_{la} discontinuity and an absence of a distinct $C_{l\max}$ peak. This is confirmed in Fig. 13c, where off-surface smoke and on-surface oil flow visualization show laminar separation close to the LE of the SD 7062 airfoil at $Re = 40,000$ (results were similar for the other airfoil

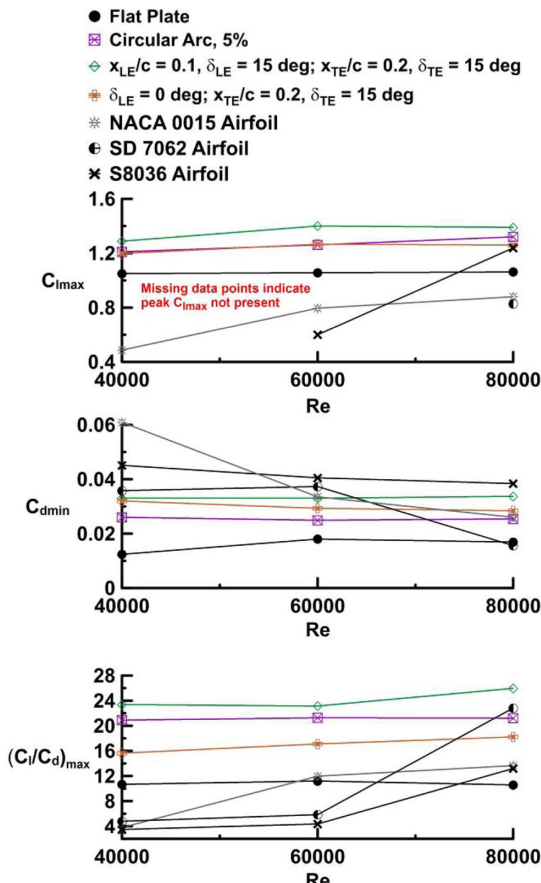


Fig. 14 Summary of aerodynamic parameters for the flat plate and conventional airfoils as affected by Reynolds number.

profiles). Increasing Re to 80,000 shows a notable performance improvement for both the S8036 and SD 7062 sections (Fig. 13b). The lift curve is more linear and shows a defined $C_{l\max}$ peak. The drag polar also shows a distinct drag rise coincident with $C_{l\max}$ —a behavior commonly associated with stall. As also shown in Fig. 13c, a LSB (which serves as the boundary-layer transition mechanism) is visible for the SD 7062 profile when the Reynolds number is raised to 80,000.

In summary, it has been shown that a thin flat plate or cambered/flapped plates are insensitive to Reynolds number within the tested range. The conventional airfoils are highly sensitive to Re , with the specific camber and thickness profile of the airfoil further complicating its Reynolds number dependence. The use of these types of conventional profiles for MAVs is problematic if the Reynolds number of operation drops below 80,000.

The effect of Reynolds number on the flat plate and airfoil geometries presented in Figs. 13a and 13b is summarized in Fig. 14. Also included are data for the TE flap set at 15 deg. The insensitivity of the flat-plate-derived airfoils to Reynolds number in this range is evident, as is the consistently superior performance of the 5% circular arc and $x_{LE}/c = 0.1$, $\delta_{LE} = \delta_{TE} = 15$ deg, and $x_{TE}/c = 0.8$ geometries. The three conventional airfoils show clear Re sensitivity. An increase in Re suggests shear layer transition, indicated by a marked $C_{l\max}$ increase coupled with a $C_{d\min}$ reduction and profound increase in the maximum lift-to-drag ratio. As a quantitative example, the increase in $(C_l/C_d)_{\max}$ associated with an increase of Re from 40,000 to 80,000 is 260, 376, and 279% for the NACA 0015, SD 7062, and S8036 airfoils, respectively.

F. Comparison of Experiment and Xfoil

Although much effort has been expended into simulating airfoils at low Reynolds number, the most commonly used tool may be Xfoil—due to its accuracy and ease of use. Consequently, Xfoil was used to simulate the tested conventional airfoils to examine its predictions against the current experimental data sets. Using the measured wind tunnel turbulence intensity of $TI = 0.24\%$, the amplification factor (n) used within Xfoil is 6, and was set accordingly during simulation.

Estimates for C_l and C_d for $Re = 40,000$ for the NACA 0015 airfoil show poor agreement (Fig. 15a). Xfoil predicts the presence of a LSB, which is not present in the experimental data. Increasing Re to 60,000 shows very good agreement with experiment. The experimental data and numerical prediction show a distinct C_l slope change at $\alpha \approx 4$ deg. The prediction of this behavior implies that Xfoil may be used as a diagnostic tool to provide insight. Xfoil predicts a LSB that migrates forward with angle of attack. The lift modulation is caused by the behavior of the displacement thickness at the TE. For $\alpha < 4$ deg, the displacement thickness is larger on the lower surface than the upper, causing apparent positive camber. This is also reflected in a predicted upper surface pressure distribution that shows greater suction levels than the inviscid case over the entire leeward surface. At approximately 4 deg angle of attack, this situation reverses, with the upper surface displacement thickness exceeding the lower surface (a result of significant boundary-layer thickening caused by the forward location of the LSB). This effectively decambers the airfoil. The drag coefficient is seen to be reasonably well-predicted for $Re \geq 60,000$ at low angles of attack.

Predictions for the S8036 and the SD 7062 airfoil (Figs. 15b and 15c) are generally less satisfactory than for the NACA 0015. Whereas the experimental data show large-scale laminar separation for $Re = 40,000$ and 60,000, the numerical predictions imply transition. The drag coefficient is generally underpredicted in all cases.

Figure 15 implies the difficulty in predicting low-Reynolds number airfoil performance, and how airfoil geometry specific the accuracy of the predictions may be.

IV. Conclusions

The performance of flapped flat plate airfoils has been characterized for Reynolds numbers ranging from 40,000 to 80,000 spanning the operational range of micro aerial vehicles (MAVs). Flap angles as well as length were varied. Measurements

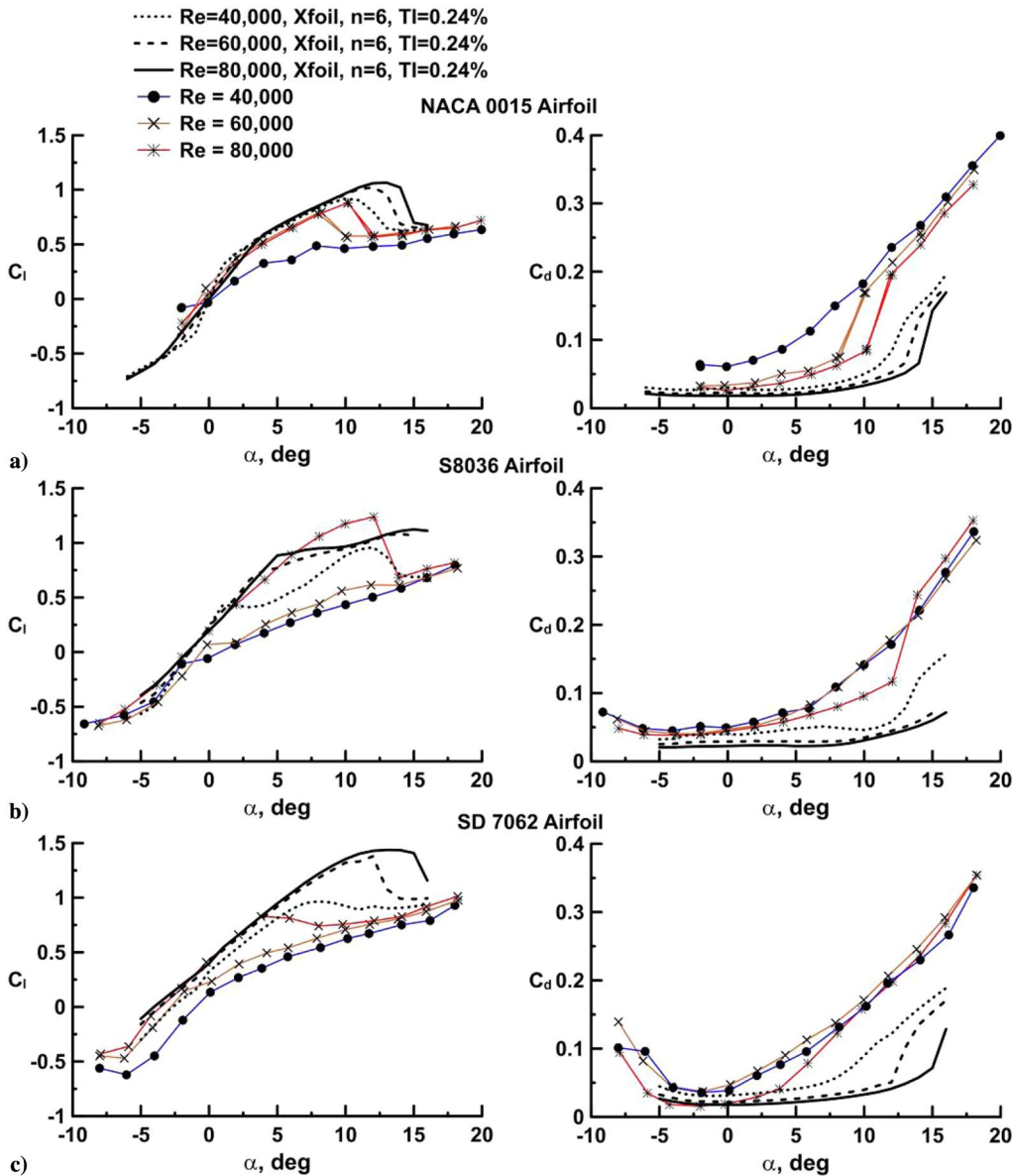


Fig. 15 Comparison of Xfoil simulations and experiment for the a) NACA 0015, b) S8036, and c) SD 7062 airfoil.

included force balance, surface pressure, as well as on and off surface flow visualization. An analytic prediction method to estimate the drag of the flapped airfoils was developed and validated. The data showed that flapped plates can improve performance significantly, in terms of maximum lift coefficient and lift-to-drag ratio. Peak lift-to-drag ratio was associated with smooth on flow onto the leading edge (LE) flap. Both the LE and trailing edge (TE) flaps reduce the drag coefficient compared with a flat airfoil, although the TE flap does it to a greater extent. The most effective flapped geometry showed an increase in the maximum lift-to-drag ratio of up to 18% compared with a 5% circular arc plate. All of the flat plate airfoils showed low sensitivity to Reynolds number within the test range. Testing of three conventional airfoils showed significant sensitivity to Reynolds number, with laminar separation dominating the flow characteristics at $Re = 40,000$ and $60,000$. The flapped flat plate airfoils demonstrated consistent and superior performance compared with the conventional airfoils and should prove effective in MAV application.

Acknowledgment

The authors would like to thank the Arizona Space Grant Consortium for support of Cory Coffman during the conduct of this research.

References

- [1] McMasters, J. H., and Henderson, M. L., "Low Speed Single-Element Airfoil Synthesis," *Technical Soaring*, Vol. 6, No. 2, 1980, pp. 1–21.
- [2] Liu, T., Kuykendoll, K., Rhew, R., and Jones, S., "Avian Wings," AIAA Paper 2004-2186, 2004.
doi:10.2514/6.2004-2186
- [3] Lissaman, P. B. S., "Low-Reynolds-Number Airfoils," *Annual Review of Fluid Mechanics*, Vol. 15, No. 1, 1983, pp. 223–239.
doi:10.1146/annurev.fl.15.010183.001255
- [4] Fisher, A. M., "The Effect of Freestream Turbulence on Fixed and Flapping Micro Air Vehicle Wings," Ph.D. Dissertation, RMIT Univ., Melbourne, Australia, 2013.
- [5] Pauley, L. L., Moin, P., and Reynolds, W. C., "The Structure of Two-Dimensional Separation," *Journal of Fluid Mechanics*, Vol. 220, No. 1, 1990, pp. 397–411.
doi:10.1017/S0022112090003317
- [6] Abdalla, I. E., and Yang, Z., "Numerical Study of the Instability Mechanism in Transitional Separating-Reattaching Flow," *International Journal of Heat and Fluid Flow*, Vol. 25, No. 4, 2004, pp. 593–605.
doi:10.1016/j.ijheatfluidflow.2004.01.004
- [7] Jones, B. M., "An Experimental Study of the Stalling of Wings," Aeronautical Research Council TR 1588, 1933.
- [8] Watmuff, J. H., "Evolution of a Wave Packet into Vortex Loops in a Laminar Separation Bubble," *Journal of Fluid Mechanics*, Vol. 397, Oct. 1999, pp. 119–169.
doi:10.1017/S0022112099006138

- [9] Traub, L. W., and Cooper, E., "Experimental Investigation of Pressure Measurement and Airfoil Characteristics at Low Reynolds Numbers," *Journal of Aircraft*, Vol. 45, No. 4, 2008, pp. 1322–1333.
doi:10.2514/1.34769
- [10] Mueller, T. J., "The Influence of Laminar Separation and Transition on Low Reynolds Number Airfoil Hysteresis," *Journal of Aircraft*, Vol. 22, No. 9, 1985, pp. 763–770.
doi:10.2514/3.45199
- [11] Withers, P. C., "An Aerodynamic Analysis of Bird Wings as Fixed Aerofoils," *Journal of Experimental Biology*, Vol. 90, 1981, pp. 143–162.
- [12] Oehme, H., and Kitzler, U., "On the Geometry of the Avian Wing (Studies on the Biophysics and Physiology of Avian Flight 11)," NASA TT-F-16901, 1975.
- [13] Laitone, E. V., "Wind Tunnel Tests of Wings at Reynolds Numbers Below 70000," *Experiments in Fluids*, Vol. 23, No. 5, 1997, pp. 405–409.
doi:10.1007/s003480050128
- [14] Hoerner, S. F., *Fluid Dynamic Lift*, Vancouver, WA, 1985, Chap. 6.
- [15] Rose, L. M., and Altman, J. M., "Low-Speed Investigation of the Stalling of a Thin Faired, Double Wedge Airfoil with Nose Flap," NACA TN 2172, Aug. 1950.
- [16] Okamoto, M., Yasuda, K., and Azuma, A., "Aerodynamic Characteristics of the Wings and Body of a Dragonfly," *The Journal of Experimental Biology*, Vol. 199, No. 2, 1996, pp. 281–294.
- [17] Cahill, J., Underwood, W. J., Nuber, R. J., and Cheesman, G. A., "Aerodynamic Forces and Loadings on Symmetrical Circular-Arc Airfoils with Plain Leading-Edge and Plain Trailing-Edge Flaps," NACA TR-1146, 1953.
- [18] Rose, L. M., and Altman, J. M., "Low-Speed Experimental Investigation of a Thin, Faired, Double-Wedge Airfoil Section with Nose and Trailing-Edge Flaps," NACA TN-1934, Aug. 1949.
- [19] Lange, R. H., "Langley Full-Scale-Tunnel Investigations of the Maximum-Lift and Stalling Characteristics of a Trapezoidal Wing of Aspect Ratio 4 with Circular-Arc Airfoil Sections," NACA TN-2823, Nov. 1952.
- [20] Traub, L. W., "Experimental Investigation of the Effect of Trailing-Edge Flaps on Delta Wings," *Journal of Aircraft*, Vol. 54, No. 5, 2017,
pp. 1945–1959.
doi:10.2514/1.C034273
- [21] Traub, L. W., "Effects of Plain and Gurney Flaps on a Nonslender Delta Wing," *Journal of Aircraft*, Vol. 56, No. 2, March 2019.
doi:10.2514/1.C034929
- [22] Glauert, M. A., "Theoretical Relationships for an Aerofoil with Hinged Flaps," ARC R&M 1095, April 1927.
- [23] Kuethe, A. M., and Chow, C., *Foundations of Aerodynamics*, 5th ed., Wiley, New York, 1998, pp. 136–154.
- [24] Traub, L. W., "Camber Effects on Minimum Power and Thrust Relations for Propeller Aircraft," *Journal of Aircraft*, Vol. 53, No. 1, 2016, pp. 299–304.
doi:10.2514/1.C033491
- [25] Houghton, E. L., Carpenter, P. W., Collicott, S., and Valentine, D., *Aerodynamics for Engineering Students*, 6th ed., Butterworth-Heinemann, U.K., March 2012, pp. 223–240.
- [26] Rinioie, K., and Stollery, J. L., "Experimental Studies of Vortex Flaps and Vortex Plates; Part 2. 1.15m Span 60 Delta Wing," National Aerospace Lab. TR-1180T, Tokyo, Oct. 1992.
- [27] Traub, L. W., "Comparative Study of Delta Wings with Blunt Leading Edges and Vortex Flaps," *Journal of Aircraft*, Vol. 33, No. 4, 1996, pp. 828–830.
doi:10.2514/3.47022
- [28] Wenzinger, C. J., and Rogallo, F. M., "Resume of Air-Loads on Slats and Flaps," NACA TN-690, March 1939.
- [29] Polhamus, E. C., "Prediction of Vortex-Lift Characteristics by a Leading Edge Suction Analogy," *Journal of Aircraft*, Vol. 8, No. 4, 1971, pp. 193–199.
doi:10.2514/3.44254
- [30] Purvis, J. W., "Analytical Prediction of Vortex Lift," *Journal of Aircraft*, Vol. 18, No. 4, 1981, pp. 225–230.
doi:10.2514/3.57485
- [31] Traub, L. W., "Analytic Drag Prediction for Cambered Wings with Partial Leading-Edge Suction," *Journal of Aircraft*, Vol. 46, No. 1, 2009, pp. 312–319.
doi:10.2514/1.38558